



Research on vibration suppression of nonlinear energy sink with linear damping and geometrically nonlinear damping

Xing-ke Qi · Jian-chao Zhang · Jun Wang · Bo-qi Li

Received: 23 November 2023 / Accepted: 12 April 2024 / Published online: 20 May 2024
© The Author(s), under exclusive licence to Springer Nature B.V. 2024

Abstract Nonlinear energy sink (NES) is a passive control device that can absorb a wide band, and it has the advantages of lightweight and strong robustness, which can play a very important role in vibration suppression. In this paper, the dynamic modeling and research on vibration suppression of NES with linear damping and geometrically nonlinear damping are carried out, and the effects of NES parameters on the vibration reduction effect are investigated. For the study of dynamic bifurcation, the slowly varying equation of the system is obtained by using the complex variable average method, and the effects of NES parameters on the number of fixed points and stability of the system are analyzed according to the slowly varying equation. At the same time, the effects of excitation amplitude and excitation frequency on the system response amplitude are also investigated. For the study of strongly modulated response (SMR), the slowly varying equation is further analyzed by using the multi-scale method, and the conditions for SMR phenomenon in the system are described by slow invariant manifold and phase portraits. By studying

the slow manifold, the detuned parameter interval for the system to appear SMR is derived. For vibration reduction performance analysis, the effects of NES parameters on vibration reduction performance are analyzed from the perspectives of energy and amplitude-frequency response, and the influence laws of various parameters on vibration suppression are revealed. The vibration reduction performance of different NES is compared and analyzed, and it is concluded that the new NES proposed in this paper has better vibration reduction performance.

Keywords Nonlinear energy sink · Complex variable average method · Strongly modulated response · Vibration suppression

1 Introduction

There are many harmful vibration problems in the fields of building structures, aviation devices and precision machinery [1, 2], which will seriously affect the use and stability of system structures, so in recent decades, scholars have been exploring methods that can effectively suppress vibrations [3–5]. At present, the structural vibration suppression methods mainly include active control, semi-active control, hybrid control and passive control. Passive control has attracted wide attention because of its low cost and simple structure in practical applications [6–8]. As a

X. Qi · J. Wang · B. Li
Department of Mechanical Engineering, Shijiazhuang
Tiedao University, Shijiazhuang 050043, China

J. Zhang (✉) · J. Wang
State Key Laboratory of Mechanical Behavior and System
Safety of Traffic Engineering Structures, Shijiazhuang
Tiedao University, Shijiazhuang 050043, China
e-mail: zjc@stdu.edu.cn

classical passive control method, NES was first proposed by Roberson, who introduced nonlinear stiffness into the traditional linear vibration absorber to form a nonlinear vibration absorber with wider vibration reduction bandwidth and better robustness [9]. The traditional NES structure is composed of viscous damping, nonlinear spring and lightweight mass block. In practical application, it can provide a special energy transfer mechanism, which is called target energy transfer (TET). TET has high energy transfer efficiency and the transfer process is unidirectional and irreversible [10, 11]. With the deepening of research, scholars have proposed more and more abundant forms of NES, such as track NES, bistable NES, lever-type NES and non-smooth NES [12–15]. Due to the complexity of both the structures for vibration reduction and the environments in which they are located, most scholars often simplify the main system into a mathematical model composed of mass block, linear damping and linear stiffness in their analysis, and on this basis, add NES to be studied for theoretical analysis [16–18]. In this paper, the main system is simplified by this method, and a dynamic model of coupled geometrically nonlinear damping NES is established.

The researchers have found that the vibration reduction performance of NES is different when the system is subjected to different excitation forms. Wang et al. [19] analyzed the vibration reduction performance of NES under impulsive excitation through experiments, while Remick et al. [20, 21] analyzed the influence of NES on system vibration suppression under impulsive excitation from the numerical aspect. Both found that NES provided good vibration reduction effect when the main system was under impulsive excitation. Zhang et al. [22] analyzed the influence of different impulsive excitation intensities on the vibration reduction performance of NES, and found that under low impulsive excitation intensities, the vibration reduction performance of traditional NES was better than that of nonlinear damping NES. Although scholars have done a lot of research on nonlinear systems under impulsive excitation, the influence law of NES parameters on vibration suppression has not been revealed.

When the system is subjected to harmonic excitation, NES will show a special steady-state response, and the amplitude of the main system will be greatly modulated. Gendelman et al. [23–25] analyzed this special response by using the complex variable average

method, and found that this special response is formed when the main system and NES have 1:1 resonance, he defined this special response as strongly modulated response. Then scholars try to use various methods to analyze whether SMR occurs in the system and the conditions that generate SMR. Starosvetsky et al. [26–28] used the multi-scale method to further analyze and used SIM to predict whether a nonlinear system would generate SMR, and found that SMR could only be generated if the system included nonlinear components. Some scholars have also found that the existence of SMR is affected by frequency detuning parameters, but the influence law has not been revealed. Kong et al. [29–31] used the main structure energy spectrum to study the vibration reduction effect of NES under harmonic excitation, focusing on the comparative analysis of the effects of different NES on the system vibration suppression. It is pointed out that NES has better vibration reduction performance than linear vibration absorber, but the effects of NES parameters on vibration suppression is not analyzed.

Previous scholars mainly focused on the effect of stiffness on the vibration reduction effect of NES, ignoring the influence of damping, so there were few studies on the analysis of NES damping [19, 32, 33]. Al-shudeifat et al. [34] studied NES with nonlinear damping and found that under high-intensity impulsive excitation, the vibration reduction performance of NES with nonlinear damping is better than that of traditional NES, and also pointed out that nonlinear damping can improve the effective stiffness and damping of the system. Jing et al. [35] studied the effect of cubic damping NES on the vibration reduction of the main system and found that cubic damping can effectively suppress the peak value near the resonance frequency. Guo et al. [36] analyzed the effect of nonlinear damping NES on the system force transmissibility and found that nonlinear damping can expand the effective bandwidth of NES. The above results indicate that damping plays an important role in the vibration reduction effect of NES.

Although researchers have conducted a lot of research on NES systems, most of these research results are on the NES stiffness, lack of research on NES damping, and lack of analytical solution verification analysis when analyzing vibration reduction applications. Based on the shortcomings of the existing research results, the model of combined damping NES is established in this paper. Firstly, the slowly varying

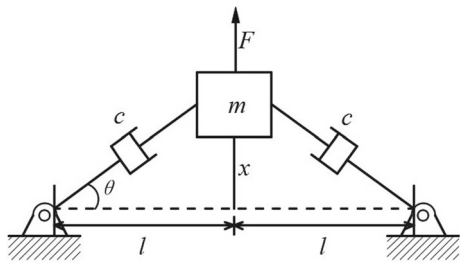


Fig. 1 Schematic diagram of geometrically nonlinear damping

equations of the system are derived by using the complex variable average method. The bifurcation characteristics of the system and the effects of excitation amplitude and frequency on the response amplitude are analyzed by the slowly varying equations. Secondly, the effects of the detuning parameters on the existence of SMR are studied by analyzing the phase portrait and the slow manifold. Finally, the vibration suppression effect of NES system under impulsive excitation is analyzed according to energy change, and the vibration suppression effect of NES system under harmonic excitation is studied according to the energy spectrum and amplitude-frequency response curve, and the optimal parameter range of NES is pointed out. The structure of this paper is as follows: the second part analyzes the bifurcation characteristics of the NES system, the third part analyzes the SMR existence interval of the NES system, the fourth part analyzes the vibration reduction effect of the NES system under impulsive excitation and harmonic excitation, and the last part summarizes the main research results of this paper.

2 Dynamic bifurcation research

The schematic diagram of geometrically nonlinear damping is shown below:

The two linear damping c horizontally are arranged symmetrically, with one end fixed and the other end connected to a small mass block m . When the mass block is moved vertically by an external force, the force generated by the linear damping of the symmetrical arrangement is nonlinear. The specific derivation process is as follows:

Let the travel distance of c under external force be δ , then the force generated by each damping can be expressed as

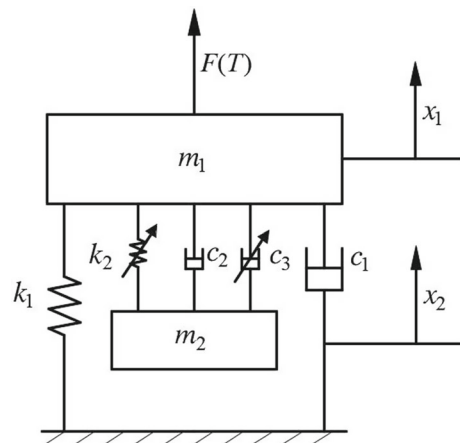


Fig. 2 The system model of NES with linear damping and geometrically nonlinear damping

$$F_1 = F_2 = c\dot{\delta} \tag{1}$$

From Fig. 1, the following geometric relationship can be obtained

$$\delta = \sqrt{x^2 + l^2}, \sin \theta = \frac{x}{\delta} = \frac{x}{\sqrt{x^2 + l^2}} \tag{2}$$

So we can get

$$F_c = 2c\dot{\delta} \sin \theta = 2cx\dot{x} \sin^2 \theta \tag{3}$$

Considering that the Angle between c and the horizontal direction is particularly small, there are

$$\sin \theta \approx \tan \theta = \frac{x}{l} \tag{4}$$

Put Eq. (4) into Eq. (3), we have

$$F_c = \frac{2c}{l^2} x^2 \dot{x} \tag{5}$$

Thus, the general form of geometrically nonlinear damping can be obtained as $x^2\dot{x}$. It is important to note that the δ should be small enough.

In this paper, a dynamic model of combined damping NES system, as shown in Fig. 2, is established. The model consists of two parts. The main system is composed of mass block m_1 , linear damping c_1 and linear stiffness spring k_1 . The nonlinear energy sink contains a smaller mass block m_2 , linear damping c_2 , geometrically nonlinear damping c_3 [37, 38] and cubic stiffness k_2 . $F(t)$ is the external excitation of the system, x_1 and x_2 are the displacements of the main system and the nonlinear energy sink, respectively.

According to Newton’s second law, the corresponding dynamic equation is established as follows

$$\begin{cases} m_1\ddot{x}_1 + c_1\dot{x}_1 + k_1x_1 + c_2(\dot{x}_1 - \dot{x}_2) + c_3(x_1 - x_2)^2 \\ \quad (\dot{x}_1 - \dot{x}_2) + k_2(x_1 - x_2)^3 = F \cos(\omega t) \\ m_2\ddot{x}_2 + c_2(\dot{x}_2 - \dot{x}_1) + c_3(x_2 - x_1)^2(\dot{x}_2 - \dot{x}_1) \\ \quad + k_2(x_2 - x_1)^3 = 0 \end{cases} \tag{6}$$

For the convenience of calculation, the following parameter transformations are introduced

$$\begin{aligned} \bar{x}_1 &= \frac{x_1}{l}, \quad \bar{x}_2 = \frac{x_2}{l}, \\ \omega_0 &= \sqrt{\frac{k_1}{m_1}}, \quad \bar{t} = t\omega_0, \quad \bar{\omega} = \frac{\omega}{\omega_0}, \\ \varepsilon &= \frac{m_2}{m_1} \ll 1, \quad \varepsilon\lambda_2 = \frac{c_2}{m_1\omega_0}, \\ \varepsilon\lambda_3 &= \frac{c_3}{m_1\omega_0}, \quad \varepsilon k = \frac{k_2}{m_1\omega_0^2}, \quad \varepsilon f = \frac{F}{lk_1} \end{aligned} \tag{7}$$

Substituting Eq. (7) into Eq. (6), and setting $c_1 = 0$. At the same time, for the convenience of subsequent writing, the overlines of $\bar{x}_1, \bar{x}_2, \bar{t}$ and $\bar{\omega}$ are omitted, and Eq. (1) is transformed into

$$\begin{cases} \ddot{x}_1 + x_1 + \varepsilon\lambda_2(\dot{x}_1 - \dot{x}_2) + \varepsilon\lambda_3(x_1 - x_2)^2(\dot{x}_1 - \dot{x}_2) \\ \quad + \varepsilon k(x_1 - x_2)^3 = \varepsilon f \cos(\omega t) \\ \ddot{x}_2 + \lambda_2(\dot{x}_2 - \dot{x}_1) + \lambda_3(x_2 - x_1)^2(\dot{x}_2 - \dot{x}_1) \\ \quad + k(x_2 - x_1)^3 = 0 \end{cases} \tag{8}$$

This paper studies the case where the ratio of external excitation frequency to the natural frequency of the system is 1:1, expressed as $\omega = 1 + \varepsilon\sigma$, where the detuning parameter σ can be used to describe the closeness between the external excitation frequency and the natural frequency of the system. Meanwhile, variable substitution is introduced into Eq. (8): $u = x_1 + \varepsilon x_2, v = x_1 - x_2, u$ represents the mass center motion and v represents the relative motion between the NES and main system.

Then the equation is transformed into

$$\begin{cases} \ddot{u} + \frac{u + \varepsilon v}{1 + \varepsilon} = \varepsilon f \cos[(1 + \varepsilon\sigma)t] \\ \ddot{v} + (1 + \varepsilon)\lambda_2\dot{v} + (1 + \varepsilon)\lambda_3v^2\dot{v} + (1 + \varepsilon)kv^3 \\ \quad + \frac{u + \varepsilon v}{1 + \varepsilon} = \varepsilon f \cos[(1 + \varepsilon\sigma)t] \end{cases} \tag{9}$$

It is not convenient to solve Eq. (9) directly, according to references [25, 30, 40], the Complex variable average method is used to solve the equation.

Introduce the following complex variable transformations.

$$\begin{aligned} \phi_1 e^{i(1+\varepsilon\sigma)t} &= \dot{u} + iu, \\ \phi_2 e^{i(1+\varepsilon\sigma)t} &= \dot{v} + iv \end{aligned} \tag{10}$$

where.

$e^{i(1+\varepsilon\sigma)t}$ indicates the fast vibrating part, ϕ_i indicates the slow modulation part.

According to Eq. (10), we have

$$\begin{aligned} u &= \frac{\phi_1 e^{i(1+\varepsilon\sigma)t} - \bar{\phi}_1 e^{-i(1+\varepsilon\sigma)t}}{2i(1 + \varepsilon\sigma)}, \quad \dot{u} = \frac{\phi_1 e^{i(1+\varepsilon\sigma)t} + \bar{\phi}_1 e^{-i(1+\varepsilon\sigma)t}}{2}, \\ \ddot{u} &= \dot{\phi}_1 e^{i(1+\varepsilon\sigma)t} + i(1 + \varepsilon\sigma) \frac{\phi_1 e^{i(1+\varepsilon\sigma)t} - \bar{\phi}_1 e^{-i(1+\varepsilon\sigma)t}}{2} \\ v &= \frac{\phi_2 e^{i(1+\varepsilon\sigma)t} - \bar{\phi}_2 e^{-i(1+\varepsilon\sigma)t}}{2i(1 + \varepsilon\sigma)}, \quad \dot{v} = \frac{\phi_2 e^{i(1+\varepsilon\sigma)t} + \bar{\phi}_2 e^{-i(1+\varepsilon\sigma)t}}{2}, \\ \ddot{v} &= \dot{\phi}_2 e^{i(1+\varepsilon\sigma)t} + i(1 + \varepsilon\sigma) \frac{\phi_2 e^{i(1+\varepsilon\sigma)t} - \bar{\phi}_2 e^{-i(1+\varepsilon\sigma)t}}{2} \end{aligned}$$

Substitute the parameter transformation into Eq. (9) and omit the fast variable part of the equation $e^{i(1+\varepsilon\sigma)t}$, the slowly varying equation of the system can be obtained as

$$\begin{cases} \dot{\phi}_1 + i\varepsilon\sigma\phi_1 + \frac{i\varepsilon(\phi_1 - \phi_2)}{2(1 + \varepsilon)} = \frac{\varepsilon f}{2} \\ \dot{\phi}_2 + i\varepsilon\sigma\phi_2 + \frac{i(\phi_2 - \phi_1)}{2(1 + \varepsilon)} + \frac{(1 + \varepsilon)\phi_2}{8} \\ \quad (4\lambda_2 + \lambda_3|\phi_2|^2 - 3ik|\phi_2|^2) = \frac{\varepsilon f}{2} \end{cases} \tag{11}$$

In order to obtain the fixed points equation of the system, the derivative term in Eq. (11) is equal to 0, which can be obtained

$$\begin{cases} i\varepsilon\sigma\phi_{10} + \frac{i\varepsilon(\phi_{10} - \phi_{20})}{2(1 + \varepsilon)} = \frac{\varepsilon f}{2} \\ i\varepsilon\sigma\phi_{20} + \frac{i(\phi_{20} - \phi_{10})}{2(1 + \varepsilon)} + \frac{(1 + \varepsilon)\phi_{20}}{8} (4\lambda_2 + \lambda_3|\phi_{20}|^2 \\ \quad - 3ik|\phi_{20}|^2) = \frac{\varepsilon f}{2} \end{cases} \tag{12}$$

The ϕ_{10} and ϕ_{20} in the formula represent the fixed points of the system and the solution of Eq. (12) can be expressed as

$$\begin{cases} \phi_{10} = \frac{\phi_{20} - i(1 + \varepsilon)f}{2(1 + \varepsilon)\sigma + 1} \\ \frac{9k^2 + \lambda_3^2}{16} |\phi_{20}|^6 + \frac{\lambda_2 \lambda_3 - 6kM\sigma}{2} |\phi_{20}|^4 \\ + (\lambda_2^2 + 4M^2\sigma^2) |\phi_{20}|^2 = M^2 f^2 \end{cases} \quad (13)$$

where $M = (2\varepsilon\sigma + 1)/(2\varepsilon\sigma + 2\sigma + 1)$. The second equation in Eq. (13) is simplified as

$$\alpha_1 Z^3 + \alpha_2 Z^2 + \alpha_3 Z = f^2 \quad (14)$$

where

$$\begin{aligned} \alpha_1 &= \frac{9k^2 + \lambda_3^2}{16M^2}, \\ \alpha_2 &= \frac{\lambda_2 \lambda_3 - 6kM\sigma}{2M^2}, \\ \alpha_3 &= \frac{\lambda_2^2 + 4M^2\sigma^2}{M^2}, \\ Z &= |\phi_{20}|^2 \end{aligned}$$

Taking the derivative of Eq. (14) yields

$$3\alpha_1 Z^2 + 2\alpha_2 Z + \alpha_3 = 0 \quad (15)$$

Equation (14) and Eq. (15) are combined to obtain the saddle-node(SN) bifurcation boundary equation of the system as follows

$$\begin{aligned} f^2 &= \alpha_1 \left(\frac{-\alpha_2 \pm \sqrt{\alpha_2^2 - 3\alpha_1\alpha_3}}{3\alpha_1} \right)^3 + \alpha_2 \left(\frac{-\alpha_2 \pm \sqrt{\alpha_2^2 - 3\alpha_1\alpha_3}}{3\alpha_1} \right)^2 \\ &\quad \alpha_3 \left(\frac{-\alpha_2 \pm \sqrt{\alpha_2^2 - 3\alpha_1\alpha_3}}{3\alpha_1} \right) \end{aligned} \quad (16)$$

According to Eq. (16), the SN bifurcation of the system is drawn, as shown in Fig. 3. Where the parameters are selected as: $\varepsilon = 0.1, k = 4/3, \lambda_2 = 0.1$ [25, 30, 40].

As can be seen from Fig. 3, the SN bifurcation boundary curve of the combined damping NES system divides the plane $[\lambda_3, f]$ into two parts, and the shape of the curve is approximately triangular. As shown in the figure above, taking points inside and outside the triangle, it can be found that there are three real roots inside the triangle and only one real root outside the triangle, indicating that there are three fixed points inside the triangle and only one fixed point outside the triangle. According to the analysis of the points taken, When f is fixed, changing the value of λ_3 can get a different number of fixed points. Similarly, when λ_3 is

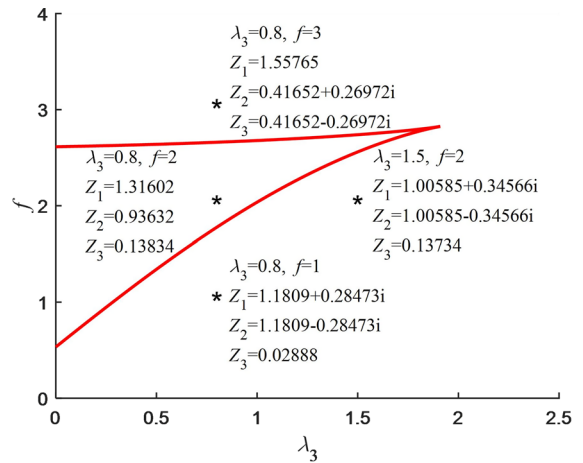


Fig. 3 SN bifurcation diagram ($\sigma = 3$)

fixed, changing the value of f can also obtain a different number of fixed points.

Next, the effects of linear damping coefficient λ_2 , mass ratio ε and detuning parameter σ on the SN bifurcation boundary curve of the system were studied. On the premise that other parameters remained unchanged, the SN bifurcation diagram of different combined damping NES parameters was obtained by changing the values of combined damping NES parameters, as shown in Fig. 4.

In Fig. 4a, the area of the SN bifurcation curve gradually decreases with the increase of the λ_2 value. In Fig. 4b, with the increase of the ε value, the area of the SN bifurcation curve gradually increases. In Fig. 4c and d, the area of the SN bifurcation curve increases with the increase of σ , regardless of whether the detuning parameter σ is greater than or less than 0. According to the above analysis, changing the linear damping coefficient λ_2 , mass ratio ε and detuning parameter σ can affect the number of fixed points.

SN bifurcation can only analyze the number of fixed points, and the stability of fixed points needs to be studied through Hopf bifurcation. Then Hopf bifurcation is used to analyze the stability of fixed points in the combined damping NES system. A small disturbance is applied to the combined damping NES system near the fixed points. Letting

$$\phi_1 = \phi_{10} + \Delta_1, \quad \phi_2 = \phi_{20} + \Delta_2 \quad (17)$$

Then Eq. (12) can be simplified to

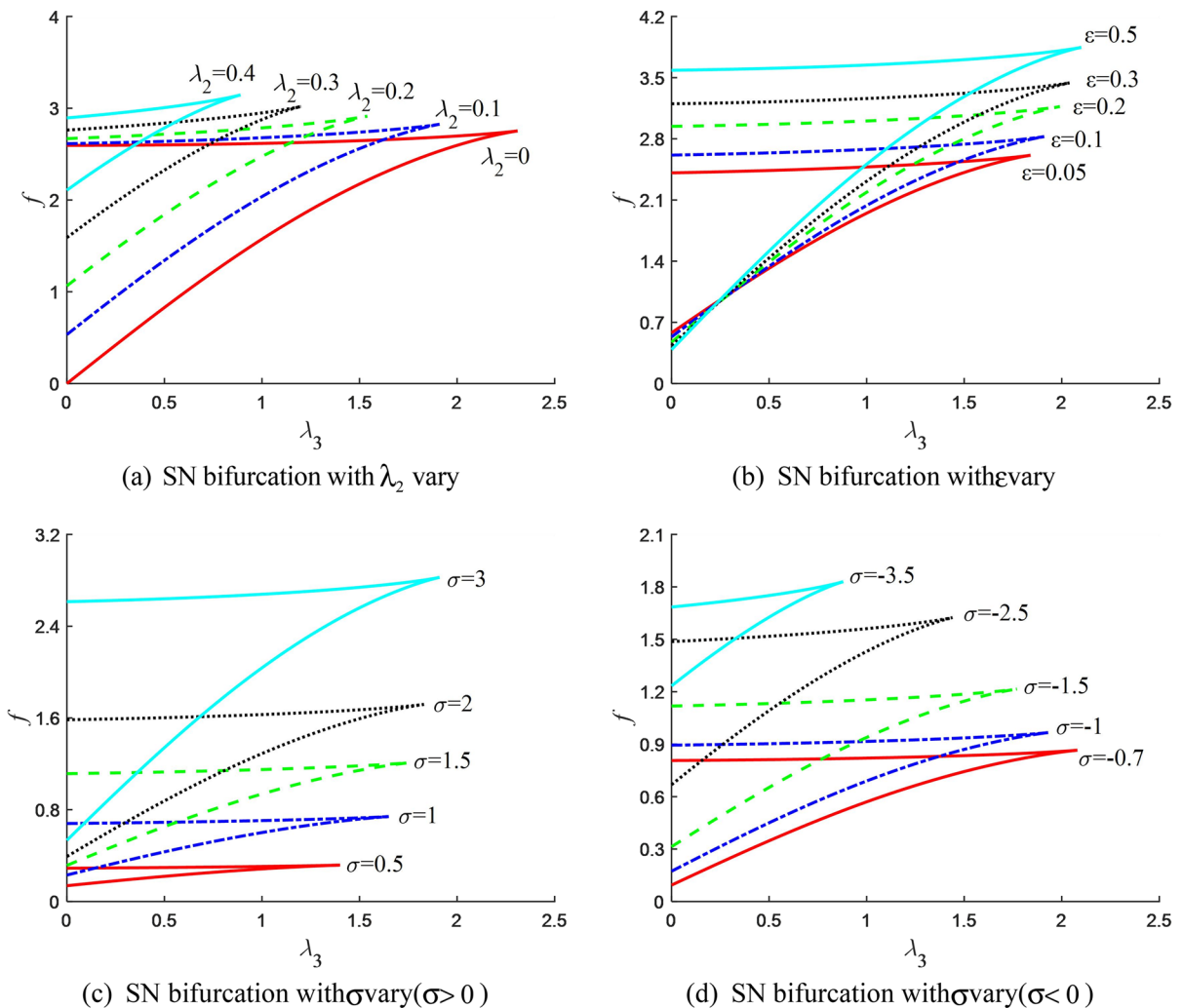


Fig. 4 SN bifurcation with combined damping NES parameters change

$$\begin{aligned}
 \dot{\Delta}_1 &= -i\varepsilon\sigma\Delta_1 - \frac{i\varepsilon}{2(1+\varepsilon)}(\Delta_1 - \Delta_2) & \dot{\Delta}_1^* &= i\varepsilon\sigma\Delta_1^* + \frac{i\varepsilon}{2(1+\varepsilon)}(\Delta_1^* - \Delta_2^*) \\
 \dot{\Delta}_2 &= -i\varepsilon\sigma\Delta_2 - \frac{i(\Delta_2 - \Delta_1)}{2(1+\varepsilon)} - \frac{(1+\varepsilon)}{2}\lambda_2\Delta_2 - \frac{(1+\varepsilon)}{4}\lambda_3|\phi_{20}|^2\Delta_2 \\
 &\quad + \frac{3ik(1+\varepsilon)}{4}|\phi_{20}|^2\Delta_2 - \frac{(1+\varepsilon)}{8}\lambda_3\phi_{20}^2\Delta_2^* + \frac{3ik(1+\varepsilon)}{8}\phi_{20}^2\Delta_2^* \\
 \dot{\Delta}_2^* &= i\varepsilon\sigma\Delta_2^* + \frac{i(\Delta_2^* - \Delta_1^*)}{2(1+\varepsilon)} - \frac{(1+\varepsilon)}{2}\lambda_2\Delta_2^* - \frac{(1+\varepsilon)}{4}\lambda_3|\phi_{20}|^2\Delta_2^* \\
 &\quad - \frac{3ik(1+\varepsilon)}{4}|\phi_{20}|^2\Delta_2^* - \frac{(1+\varepsilon)}{8}\lambda_3\phi_{20}^{*2}\Delta_2 - \frac{3ik(1+\varepsilon)}{8}\phi_{20}^{*2}\Delta_2
 \end{aligned} \tag{18}$$

The characteristic polynomial of the above equation can be expressed as

$$\mu^4 + \gamma_1\mu^3 + \gamma_2\mu^2 + \gamma_3\mu + \gamma_4 = 0 \tag{19}$$

where

$$\begin{aligned}
 \gamma_1 &= \frac{(1+\varepsilon)}{2}(2\lambda_2 + \lambda_3Z) & \gamma_2 &= \frac{3(1+\varepsilon)^2(9k^2 + \lambda_3^2)}{64}Z^2 \\
 &\quad + \frac{-3(1+2\sigma+2\varepsilon^2\sigma)k + (1+\varepsilon)^2\lambda_2\lambda_3}{4}Z \\
 &\quad \frac{1+4\varepsilon\sigma+8\varepsilon^2\sigma^2+(1+\varepsilon)^2\lambda_2^2}{4} \\
 \gamma_3 &= \frac{\varepsilon}{8}(2\lambda_2 + \lambda_3Z)(1+4\varepsilon\sigma+4\varepsilon\sigma^2+4\varepsilon^2\sigma^2) \\
 \gamma_4 &= \frac{3\varepsilon^2(1+2\sigma+2\varepsilon\sigma)^2(9k^2 + \lambda_3^2)}{256}Z^2 \\
 &\quad + \left[\frac{\varepsilon^2(1+2\sigma+2\varepsilon\sigma)^2}{16}\lambda_2\lambda_3 - \frac{3k\varepsilon^2\sigma(1+2\varepsilon\sigma)(1+2\sigma+2\varepsilon\sigma)}{8} \right] Z \\
 &\quad + \varepsilon^2 \frac{4\sigma^2(1+2\varepsilon\sigma)^2 + \lambda_3^2(1+2\sigma+2\varepsilon\sigma)^2}{16}Z = |\phi_{20}|^2
 \end{aligned} \tag{20}$$

When the stability of the fixed points changes, the eigenvalues of the system cross the imaginary part of the complex plane, so there is the following condition.

$$\mu = \pm i\Omega \tag{21}$$

Substituting Eq. (21) into Eq. (19), we get

$$v_1 Z^2 + v_2 Z + v_3 = 0 \tag{22}$$

where

$$\begin{aligned} v_1 &= 3(1 + \varepsilon)^2(9k^2 + \lambda_3^2) \\ v_2 &= 16(1 + \varepsilon)[(1 + \varepsilon)\lambda_2\lambda_3 - 3k(1 + 4\varepsilon\sigma)] \\ v_3 &= 16[(1 + 4\varepsilon\sigma)^2 + \lambda_2^2(1 + \varepsilon)^2] \end{aligned} \tag{23}$$

By solving Eq. (22), we can obtain

$$Z_{1,2} = \frac{-v_2 \pm \sqrt{v_2^2 - 4v_1v_3}}{2v_1} \tag{24}$$

Combined with Eq. (14), the Hopf bifurcation boundary equation of the system is obtained as follows

$$\begin{aligned} f^2 &= \alpha_1 \left(\frac{-v_2 \pm \sqrt{v_2^2 - 4v_1v_3}}{2v_1} \right)^3 + \alpha_2 \left(\frac{-v_2 \pm \sqrt{v_2^2 - 4v_1v_3}}{2v_1} \right)^2 \\ &\quad \alpha_3 \left(\frac{-v_2 \pm \sqrt{v_2^2 - 4v_1v_3}}{2v_1} \right) \end{aligned} \tag{25}$$

According to Eq. (16) and (25), the bifurcation diagrams of the combined damping NES system are presented in Fig. 5.

In Fig. 5, the solid line represents the SN bifurcation curve and the dashed line represents the Hopf bifurcation curve. The region enclosed by the Hopf bifurcation curve of the system and the Y-axis is the unstable region of the fixed points, and the external region is the stable region. As can be seen from Fig. 5, the region where the SN bifurcation curve of the system intersects with the Hopf bifurcation curve, shows that the system is affected by two kinds of bifurcation in some areas. When the selected parameters are located outside the two bifurcation curves, only a single stable fixed point can appear in the system.

At the same time, this paper studies the effects of linear damping coefficient λ_2 , mass ratio ε and detuning parameter σ on the Hopf bifurcation curve of the system. On the premise that other parameters remain unchanged, the Hopf bifurcation diagram of different combined damping NES parameters is

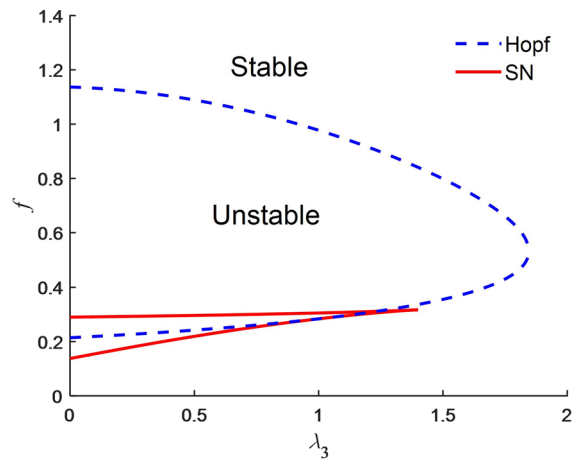


Fig. 5 SN bifurcation and Hopf bifurcation diagrams of the system

obtained by changing the values of combined damping NES parameters, as shown in Fig. 6.

It can be seen from Fig. 6 that changes in the linear damping coefficient λ_2 , mass ratio ε and the detuning parameter σ will result in changes in the Hopf bifurcation curve of the system similar to that of the SN bifurcation, indicating that the effects of changing combined damping NES parameters on the number and stability of fixed points is similar.

Figure 7 plots the effects of external excitation amplitude change and frequency change on the system response amplitude, respectively.

It can be seen from Fig. 7 that no matter whether the excitation frequency changes or the excitation amplitude changes, the state of the system changes from a stable state to an unstable state, and finally returns to a stable state, representing that the number of fixed points changes from a single to three stages, and finally returns to a single stage. In Fig. 7a, the response amplitude of the system has a high-amplitude response loop in the frequency range of (-1.14, -0.51), which is caused by SN bifurcation. SN bifurcation also occurs in the frequency range (0.77, 1.15), and Hopf bifurcation occurs in the frequency range (-0.48, 1.15). This diagram is a good validation of the bifurcation in Figs. 4 and 6.

Through the analysis of the bifurcation characteristics of the system, it can be seen that adjusting combined damping NES parameters can make the system in an unstable state and smaller response amplitude of the system, which is important for suppressing the system vibration.

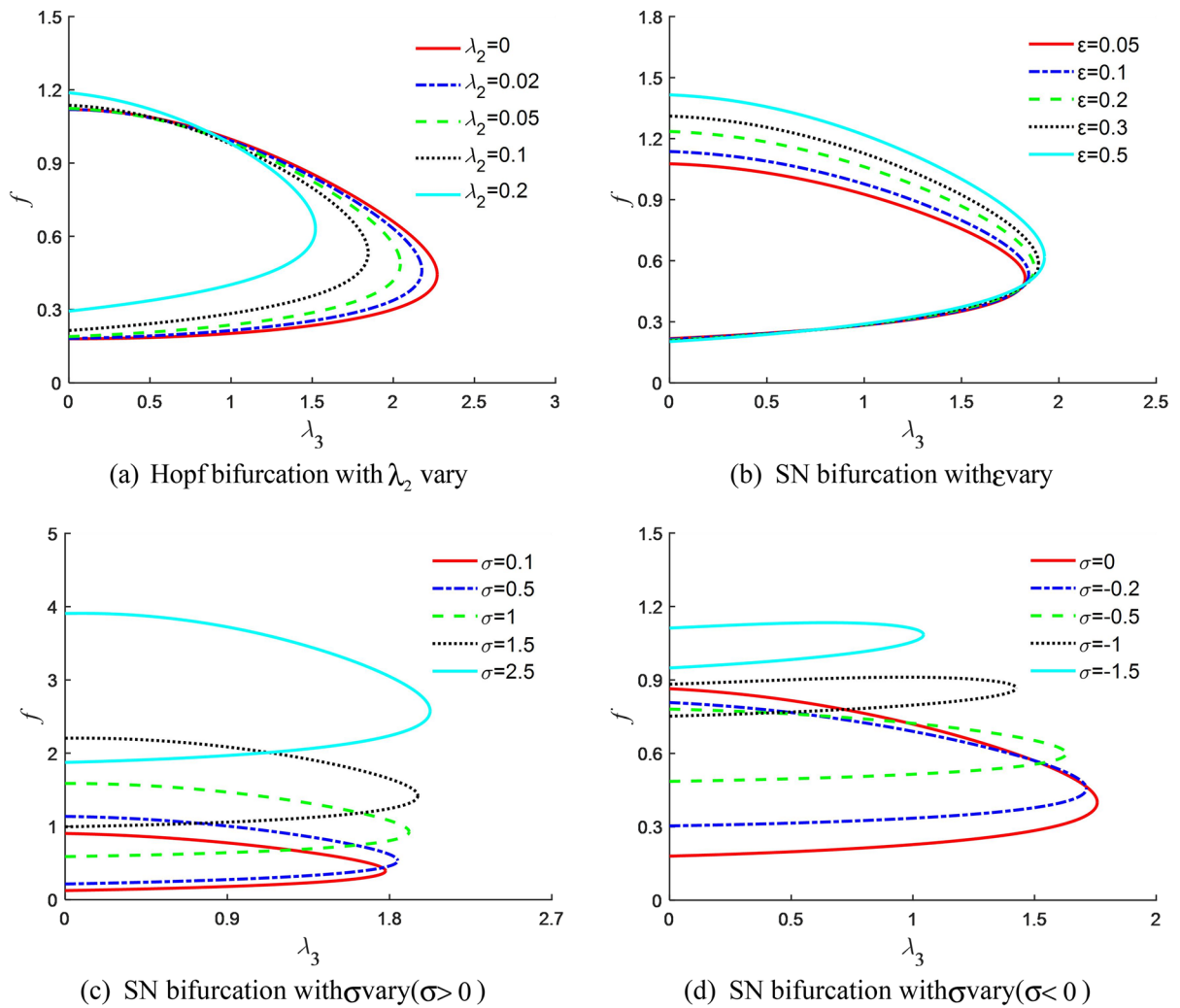


Fig. 6 Hopf bifurcation with combined damping NES parameters change

3 Strongly modulated response analysis

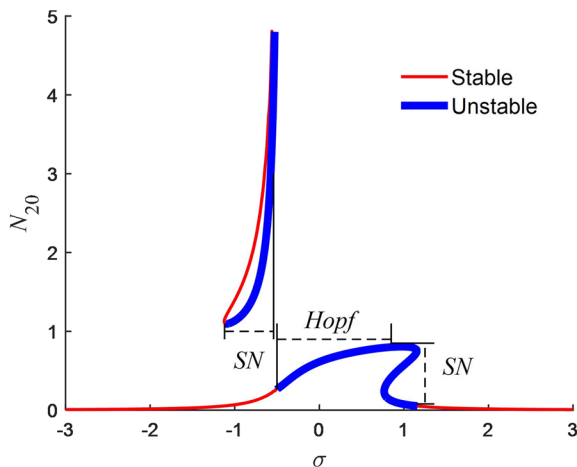
The current research results show that SMR occurs at the resonance frequency of the system, and when SMR occurs, the vibration suppression effect of combined damping NES on the system can be greatly improved. The purpose of this section is to determine the frequency interval in which the system generates SMR.

According to Eq. (11), this system is a four-dimensional phase space $(\phi_1, \dot{\phi}_1, \phi_2, \dot{\phi}_2)$, slow converter consists of 4 variables, where ϕ_2 and $\dot{\phi}_2$ are fast variables, ϕ_1 and $\dot{\phi}_1$ are slow variables. In order to facilitate subsequent calculation, Eq. (11) is processed to reduce the number of variables in the phase

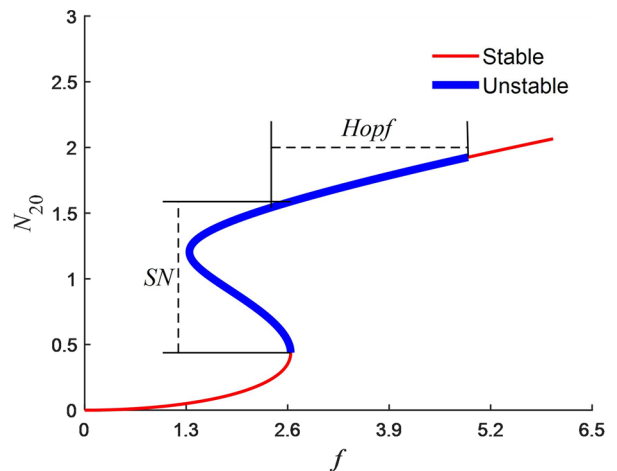
plane of the equation. The reduced equation of this system is obtained as follows

$$\ddot{\phi}_2 + \frac{d}{dt} \left[\frac{i(1 + 4\varepsilon\sigma)}{2} \phi_2 + \frac{(1 + \varepsilon)\phi_2}{8} \left(4\lambda_2 + \lambda_3|\phi_2|^2 - 3ik|\phi_2|^2 \right) \right] + \phi_2 \left[-\frac{\varepsilon\sigma}{2}(1 + 2\varepsilon\sigma) + \frac{i\varepsilon(1 + 2\sigma + 2\varepsilon\sigma)}{16} \left(4\lambda_2 + \lambda_3|\phi_2|^2 - 3ik|\phi_2|^2 \right) \right] - \frac{i\varepsilon f}{4}(1 + 2\varepsilon\sigma) = 0 \tag{26}$$

We use the multi-scale method to solve Eq. (11). Defining



(a) The influence diagram of the response amplitude when the excitation frequency change



(b) The influence diagram of the response amplitude when the excitation amplitude change

Fig. 7 System response amplitude

$$\begin{aligned} \phi_2 &= \phi_2(t_0, t_1, \dots), t_n = \varepsilon^n t, n = 0, 1, \dots \\ D &= D_0 + \varepsilon D_1 + \dots = \frac{\partial}{\partial t_0} + \varepsilon \frac{\partial}{\partial t_1} + \dots \end{aligned} \tag{27}$$

The Eq. (26) can be converted to

$$\begin{aligned} \varepsilon^0 : D_0^2 \phi_2 + \frac{D_0 \phi_2}{8} (4i + 4\lambda_2 + \lambda_3 |\phi_2|^2 - 3ik |\phi_2|^2) &= 0 \\ \varepsilon^1 : 2D_0 D_1 \phi_2 + \frac{D_0 \phi_2}{8} (16i\sigma + 4\lambda_2 + \lambda_3 |\phi_2|^2 - 3ik |\phi_2|^2) \\ + \frac{D_1 \phi_2}{8} (4i + 4\lambda_2 + \lambda_3 |\phi_2|^2 - 3ik |\phi_2|^2) - \frac{\sigma}{2} \phi_2 \\ + \frac{i(1 + 2\sigma)\phi_2}{16} (4\lambda_2 + \lambda_3 |\phi_2|^2 - 3ik |\phi_2|^2) - \frac{if}{4} &= 0 \end{aligned} \tag{28}$$

By integrating the first formula of the above equation, we can get

$$D_0 \phi_2 + \frac{\phi_2}{8} (4i + 4\lambda_2 + \lambda_3 |\phi_2|^2 - 3ik |\phi_2|^2) = C(t_1, \dots) \tag{29}$$

Setting $D_0 \phi_2 = 0$, the equation of the system at the fixed point can be obtained as

$$\frac{\phi_2}{8} (4i + 4\lambda_2 + \lambda_3 |\phi_2|^2 - 3ik |\phi_2|^2) = C(t_1) \tag{30}$$

Since ϕ_2 is only related to t_1 , introduce: $\phi_2(t_1) = N(t_1)e^{i\theta(t_1)}$, put it into (30), there is

$$\frac{9k^2 + \lambda_3^2}{16} N^6 + \frac{\lambda_2 \lambda_3 - 3k}{2} N^4 + (1 + \lambda_2^2) N^2 = 4|C|^2 \tag{31}$$

Letting $Z = N_2$, substituting it into (31) and derivation, one obtains

$$\frac{27k^2 + 3\lambda_3^2}{16} Z^2 + (\lambda_2 \lambda_3 - 3k)Z + \lambda_2^2 + 1 = 0 \tag{32}$$

The solutions of Eq. (32) are as follows

$$\begin{aligned} Z_{1,2} &= \frac{4(6k - 2\lambda_2 \lambda_3) \mp 4\sqrt{k^2(9 - 27\lambda_2^2) - 24k\lambda_2 \lambda_3 + \lambda_3^2(-3 + \lambda_2^2)}}{3(9k^2 + \lambda_3^2)} \Rightarrow \\ N_{1,2} &= \sqrt{\frac{4(6k - 2\lambda_2 \lambda_3) \mp 4\sqrt{k^2(9 - 27\lambda_2^2) - 24k\lambda_2 \lambda_3 + \lambda_3^2(-3 + \lambda_2^2)}}{3(9k^2 + \lambda_3^2)}} \end{aligned} \tag{33}$$

According to the solutions of Eqs. (31) and (33), the corresponding coordinate equation of the starting and landing point of the system where the jump phenomenon occurs can be obtained as follows

$$\begin{aligned} \frac{9k^2 + \lambda_3^2}{16} Z_{1,2}^3 + \frac{\lambda_2 \lambda_3 - 3k}{2} Z_{1,2}^2 + (1 + \lambda_2^2) Z_{1,2} \\ = \frac{9k^2 + \lambda_3^2}{16} Z_{u,d}^3 + \frac{\lambda_2 \lambda_3 - 3k}{2} Z_{u,d}^2 + (1 + \lambda_2^2) Z_{u,d} \end{aligned} \tag{34}$$

The solutions of Eq. (34) are as follows

$$\begin{aligned} Z_{u,d} &= \frac{4(6k - 2\lambda_2 \lambda_3) \pm 8\sqrt{k^2(9 - 27\lambda_2^2) - 24k\lambda_2 \lambda_3 + \lambda_3^2(-3 + \lambda_2^2)}}{3(9k^2 + \lambda_3^2)} \Rightarrow \\ N_{u,d} &= \sqrt{\frac{4(6k - 2\lambda_2 \lambda_3) \pm 8\sqrt{k^2(9 - 27\lambda_2^2) - 24k\lambda_2 \lambda_3 + \lambda_3^2(-3 + \lambda_2^2)}}{3(9k^2 + \lambda_3^2)}} \end{aligned} \tag{35}$$

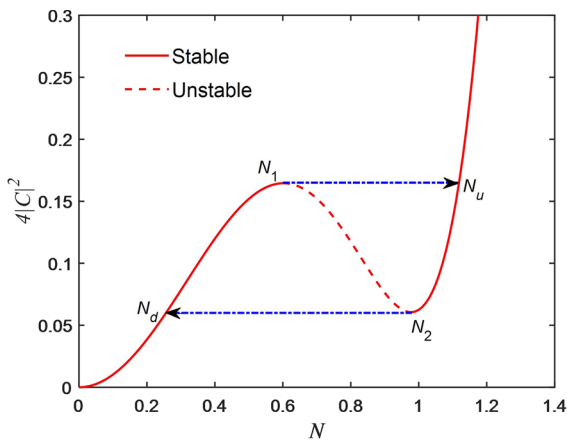


Fig. 8 SIM projection

$N_{1,2}$ indicate the extreme value point of the SIM of the system, which represents the return point of the SIM, and determines the position where the SIM of the system may jump. Combined with Eq. (31), select $k = 4/3$, $\lambda_2 = \lambda_3 = 0.2$ [19], and draw the SIM of the system as shown.

In Fig. 8, the dotted line with an arrow represents the jump trajectory between the left and right stable parts of the system. Since the slow-varying amplitude of the system is affected by manifold invariance, it can only move along the SIM curve. When the slow-varying amplitude moves along the curve of the left stable part to N_1 , because the dotted line between the two return points is the unstable part, the system will not move along the SIM to N_2 , but directly jump from N_1 to N_u , and then continue to move along the right stable part. When moving to N_2 , for the same reason, the slow-varying amplitude of the system jumps directly to point N_d , and then continues along the left stable part. This process creates a continuous jump, the jumping process is manifested as: $N_1 \rightarrow N_u \rightarrow N_2 \rightarrow N_d \rightarrow N_1$. This continuous jumping process makes it possible for SMR to appear in the system.

Next, the first-order equation in Eq. (31) is further analyzed to study the dynamic characteristics of the system tending to stability on time scale t_0 . When $t_0 \rightarrow \infty$, the first order equation can be converted to

$$\frac{D_1 \phi_2}{8} (4i + 4\lambda_2 + \lambda_3 |\phi_2|^2 - 3ik |\phi_2|^2) = T \tag{36}$$

where

$$T = \frac{if}{4} + \frac{\sigma}{2} \phi_2 - \frac{i(1+2\sigma)\phi_2}{16} (4\lambda_2 + \lambda_3 |\phi_2|^2 - 3ik |\phi_2|^2) \tag{37}$$

Take complex conjugation of Eq. (36) and combine Eq. (34), we can get

$$\frac{\partial \phi_2}{\partial t_1} = \frac{T [-2i + 2\lambda_2 + (\lambda_3 + 3ik) |\phi_2|^2] - \frac{T}{2} (\lambda_3 - 3ik) \phi_2^2}{\frac{27k^2 + 3\lambda_3^2}{16} |\phi_2|^4 + (\lambda_2 \lambda_3 - 3k) |\phi_2|^2 + \lambda_2^2 + 1} \tag{38}$$

Introducing complex variables to Eq. (37) and Eq. (38), one has

$$\begin{cases} G(N) \frac{\partial N}{\partial t_1} = -\frac{\lambda_3 N^3}{4} + \frac{fN^2}{4} (\lambda_3 \sin \theta - 3k \cos \theta) \\ \quad + \lambda_2 (f \sin \theta - N) + f \cos \theta \\ G(N) \frac{\partial \theta}{\partial t_1} = -\frac{3N^4}{16} (9k^2 + \lambda_3^2) (1 + 2\sigma) \\ \quad + \left[\frac{3k}{4} (1 + 8\sigma) - (1 + 2\sigma) \lambda_2 \lambda_3 \right] N^2 + \\ \quad \frac{3fN}{4} (\lambda_3 \cos \theta + 3k \sin \theta) + \frac{f}{N} (\lambda_2 \cos \theta - \sin \theta) \\ \quad - [\lambda_2^2 (1 + 2\sigma) + 2\sigma] \end{cases} \tag{39}$$

where

$$G(N) = 2 \left[\frac{27k^2 + 3\lambda_3^2}{16} N^4 + (\lambda_2 \lambda_3 - 3k) N^2 + \lambda_2^2 + 1 \right] \tag{40}$$

When jumping occurs, fold line will appear in the system. In order to avoid singularity in the system, Eq. (39) is simplified as

$$\begin{cases} N' = -\frac{\lambda_3 N^3}{4} + \frac{fN^2}{4} (\lambda_3 \sin \theta - 3k \cos \theta) \\ \quad + \lambda_2 (f \sin \theta - N) + f \cos \theta \\ \theta' = -\frac{3N^4}{16} (9k^2 + \lambda_3^2) (1 + 2\sigma) \\ \quad + \left[\frac{3k}{4} (1 + 8\sigma) - (1 + 2\sigma) \lambda_2 \lambda_3 \right] N^2 + \\ \quad \frac{3fN}{4} (\lambda_3 \cos \theta + 3k \sin \theta) + \frac{f}{N} (\lambda_2 \cos \theta - \sin \theta) \\ \quad - [\lambda_2^2 (1 + 2\sigma) + 2\sigma] \end{cases} \tag{41}$$

Equation (41) defines the phase portrait of the system on plane $[\theta, N]$, the parameters are selected as: $k = 4/3$, $\lambda_2 = \lambda_3 = 0.2$, $f = 1$, integrates the above equation, and draws the phase portraits of the system under different σ , as shown in Fig. 9. The two vertical lines in Fig. 9 define the initial phase angle interval for the SIM to jump, which is called the phase jump interval. θ_1 and θ_2 represent the initial phase angle of the N_1 and N_2 . The two horizontal lines correspond to the jump trajectory of the two return points in Fig. 8, and the blank area between them corresponds to the

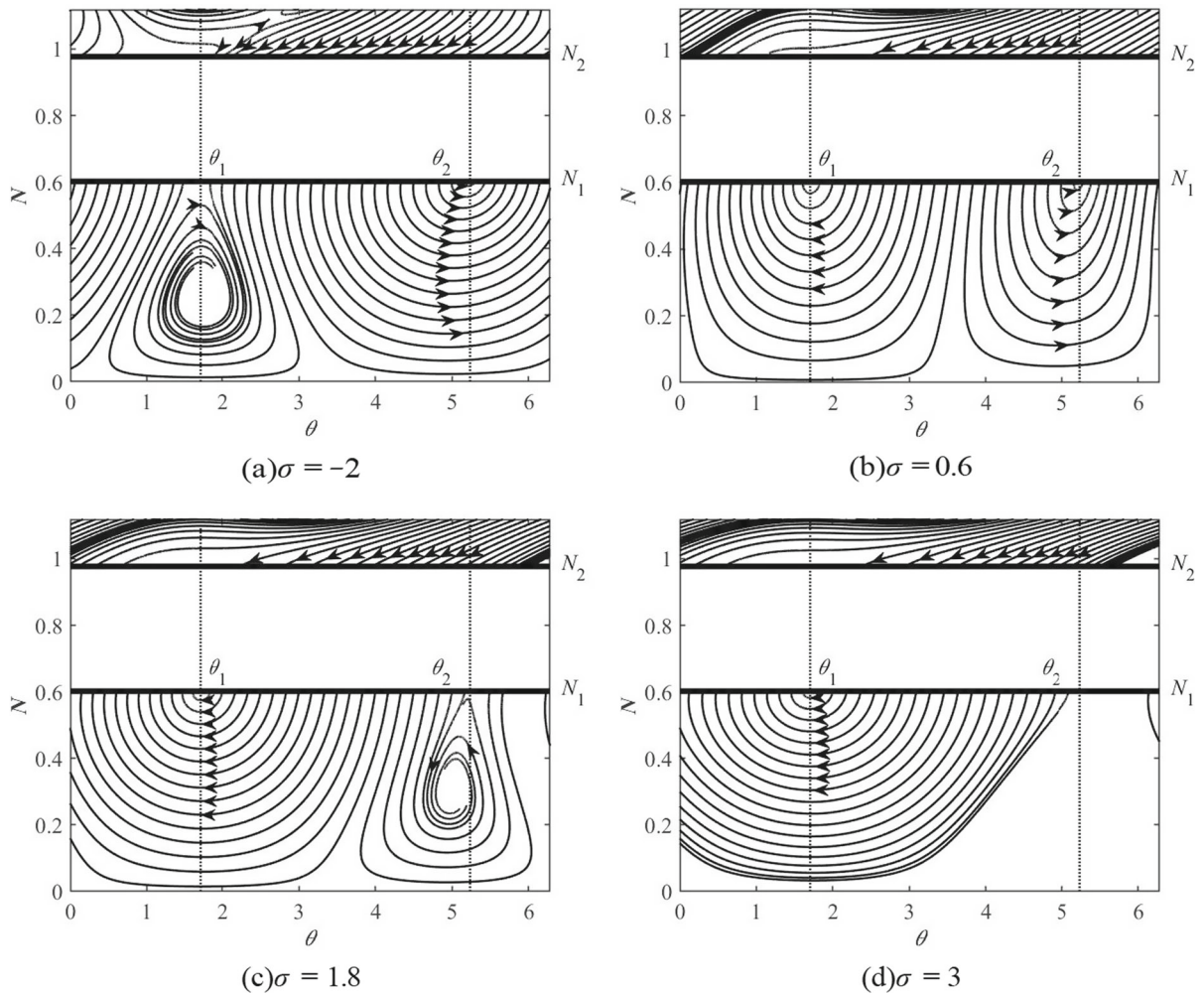


Fig. 9 Phase portraits with σ change

unstable part in Fig. 8. The arrow represents the future direction of the phase portrait motion.

As can be seen from Fig. 9, the motion path of the phase portraits starts from N_1 within the jump interval, moves down along the arrow, and returns to N_1 outside the jump interval. However, a part of the phase portraits cannot return to N_1 due to the presence of attractors, as shown in Fig. 9a and c, which will converge this part of the phase portraits. Those that return to N_1 produce a jump, crossing the unstable part between the two horizontal lines to N_2 , then moving up the phase portrait and back to N_2 within the jump interval, and finally jumping from N_2 to N_1 , forming a complete jump process, which corresponds to the change in Fig. 8. The continuous motion process of the above phase portraits provide the possibility for

SMR to occur in the system, but whether the system occur SMR needs further analysis.

Since the phase portraits cannot clearly indicate whether the system generates SMR, and the jumping process of the phase portrait is extremely complex and unstable, one-dimensional mapping is often used to analyze the detuning parameter interval of the system where SMR occurs [39]. However, one-dimensional mapping cannot intuitively distinguish the mapping lines that generate SMR phenomenon. At the same time, it is easy to produce errors when calculating jump points, so the slow manifold is used in this paper to intuitively study the detuning parameter interval of the system that generates SMR phenomenon.

Considering the first two orders of the time scale, setting

$$\phi_1(t) = a_1(t) + ib_1(t), \quad \phi_2(t) = a_2(t) + ib_2(t) \quad (42)$$

By substituting Eq. (42) into Eq. (11) and taking ε^0 to separate the real and imaginary parts, the system of ordinary differential equations can be obtained as

$$\begin{cases} \dot{a}_1 = \varepsilon\sigma b_1 + \frac{\varepsilon(b_1 - b_2)}{2(1 + \varepsilon)} + \frac{\varepsilon f}{2} \\ \dot{b}_1 = -\varepsilon\sigma a_1 - \frac{\varepsilon(a_1 - a_2)}{2(1 + \varepsilon)} \\ \dot{a}_2 = \varepsilon\sigma b_2 + \frac{(b_2 - b_1)}{2(1 + \varepsilon)} - \frac{(1 + \varepsilon)[4\lambda_2 + \lambda_3(a_2^2 + b_2^2)]a_2}{8} \\ \quad - \frac{3k(1 + \varepsilon)(a_2^2 + b_2^2)b_2}{8} + \frac{\varepsilon f}{2} \\ \dot{b}_2 = -\varepsilon\sigma a_2 - \frac{(a_2 - a_1)}{2(1 + \varepsilon)} - \frac{(1 + \varepsilon)[4\lambda_2 + \lambda_3(a_2^2 + b_2^2)]b_2}{8} \\ \quad + \frac{3k(1 + \varepsilon)(a_2^2 + b_2^2)a_2}{8} \end{cases} \quad (43)$$

Using Matlab to solve Eqs. (43), parameters are selected as $k = 4/3$, $\lambda_2 = \lambda_3 = 0.2$, $f = 1$, and the slow manifolds of the system response are drawn, as shown in Fig. 10.

As can be seen from Fig. 10, when $\sigma = -2$, although the slow manifold of the system increases from 0 to N_1 , it does not jump to N_2 . Instead, after experiencing several periodic changes, it is attracted by the lower attractor to the lower stable branch, forming a local cycle. At this time, the system was unable to generate SMR. When $\sigma = -0.9$, although the slow manifold of the system can reach N_1 and jump to N_2 , it does not return from N_2 to N_1 , but is attracted by the attractor above and cannot form a complete cycle. At this time, the system is also unable to generate a complete SMR. When $\sigma = 1$, the slow manifold of the system can form a complete jump loop between N_1 and N_2 , and at this time, the system can exhibit stable SMR. When $\sigma = 2.1$, the changes of the slow manifold of the system, as shown in Fig. 10a, are all attracted to the lower stable branch by the lower attractor, which cannot form a complete jump loop, so the system cannot generate SMR.

In order to verify the correctness of using the slow manifold to analyze SMR in the system, this paper uses the time response diagram for comparison and verification. Under the premise of ensuring the same parameter selection, the time response diagrams of the main system under different σ are drawn, as shown in Fig. 11.

The time response diagram in Fig. 11 corresponds to the slow manifold diagram in Fig. 10. Observing the above figure, it can be seen that it is reliable to analyze the occurrence of SMR in the system through the slow manifold. Because the calculation of the slow manifold is simpler and the observation of the slow manifold is easier than one-dimensional mapping, it is easy to determine the detuning parameter interval of SMR in the system by the slow manifold. After calculation, the interval of SMR in this example is $[-0.19, 1.52]$.

Figure 12 plots the slow manifold diagrams of the system response under different ε .

As can be seen from Fig. 12, when ε changes, the shape of the slow manifold of the system basically does not change, and with the decrease of ε , the numerical solution of the slow manifold corresponds better with the analytical solution, with a higher degree of agreement. This indicates that it is easier to determine whether SMR occurs in the system by selecting a small ε .

4 Vibration reduction performance analysis

4.1 Energy analysis

This section will study the vibration suppression effect of combined damping NES on the main system through the numerical solution, and the vibration reduction analysis and comparison will be carried out from the perspective of energy, further explaining the vibration reduction effect of the proposed combined damping NES in this paper. Firstly, the energy variation of a system containing combined damping NES under impulsive excitation is studied. According to Eq. (6), the dynamic equation under impulsive excitation can be obtained as

$$\begin{cases} \ddot{x}_1 + x_1 + \varepsilon\lambda_2(\dot{x}_1 - \dot{x}_2) + \varepsilon\lambda_3(x_1 - x_2)^2(\dot{x}_1 - \dot{x}_2) \\ \quad + \varepsilon k(x_1 - x_2)^3 = \varepsilon A\delta(t) \\ \ddot{x}_2 + \lambda_2(\dot{x}_2 - \dot{x}_1) + \lambda_3(x_2 - x_1)^2(\dot{x}_2 - \dot{x}_1) \\ \quad + k(x_2 - x_1)^3 = 0 \end{cases} \quad (44)$$

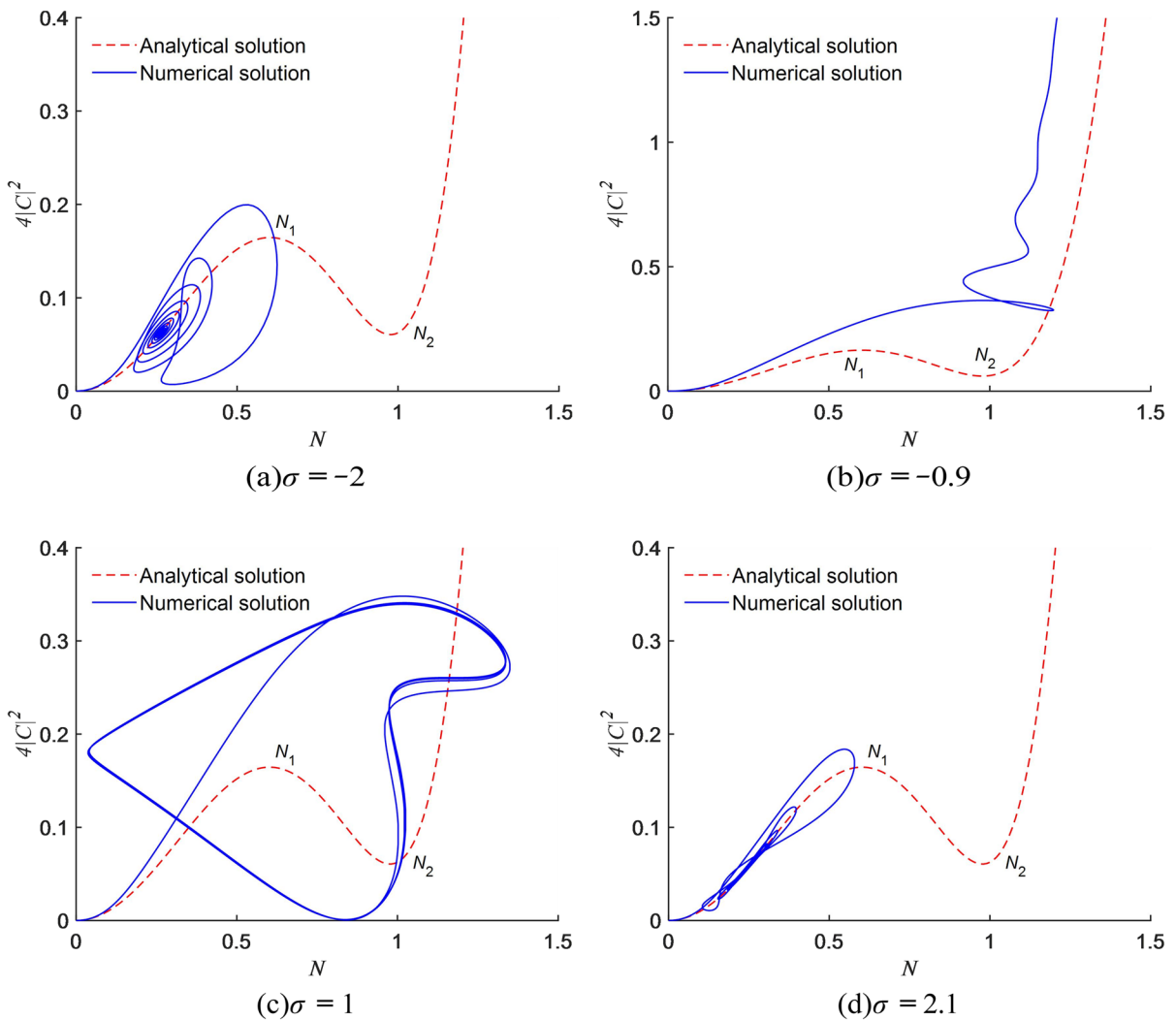


Fig. 10 Slow manifolds of the system response with σ change

According to the momentum theorem, applying impulsive excitation to the system is equivalent to an initial velocity provided to the main system, then the initial conditions of the combined damping NES system are $x_1(0) = x_2(0) = \dot{x}_2(0) = 0, \dot{x}_1(0) = Am/s$.

The energy of the main system is denoted by E_1 and is defined as

$$E_1 = \frac{1}{2}\dot{x}_1^2 + \frac{1}{2}x_1^2 \tag{45}$$

The energy of combined damping NES is denoted by E_2 and is defined as

$$E_2 = \frac{1}{2}\varepsilon\dot{x}_2^2 + \frac{1}{4}\varepsilon k(x_1 - x_2)^4 \tag{46}$$

The total energy E of the system consists of E_1 and E_2 . The expression is as

$$E = E_1 + E_2 = \frac{1}{2}(\dot{x}_1^2 + \varepsilon\dot{x}_2^2) + \frac{1}{2}\left[x_1^2 + \frac{1}{2}\varepsilon k(x_1 - x_2)^4\right] \tag{47}$$

By substituting the initial conditions into E , the initial energy E_0 of the system under impulsive excitation can be obtained as

$$E_0 = \frac{1}{2}\dot{x}_1^2 = \frac{1}{2}A^2 \tag{48}$$

System parameters are selected as: $k = 4/3, \lambda_2 = \lambda_3 = 0.3, \varepsilon = 0.1$ [19]. The time response and

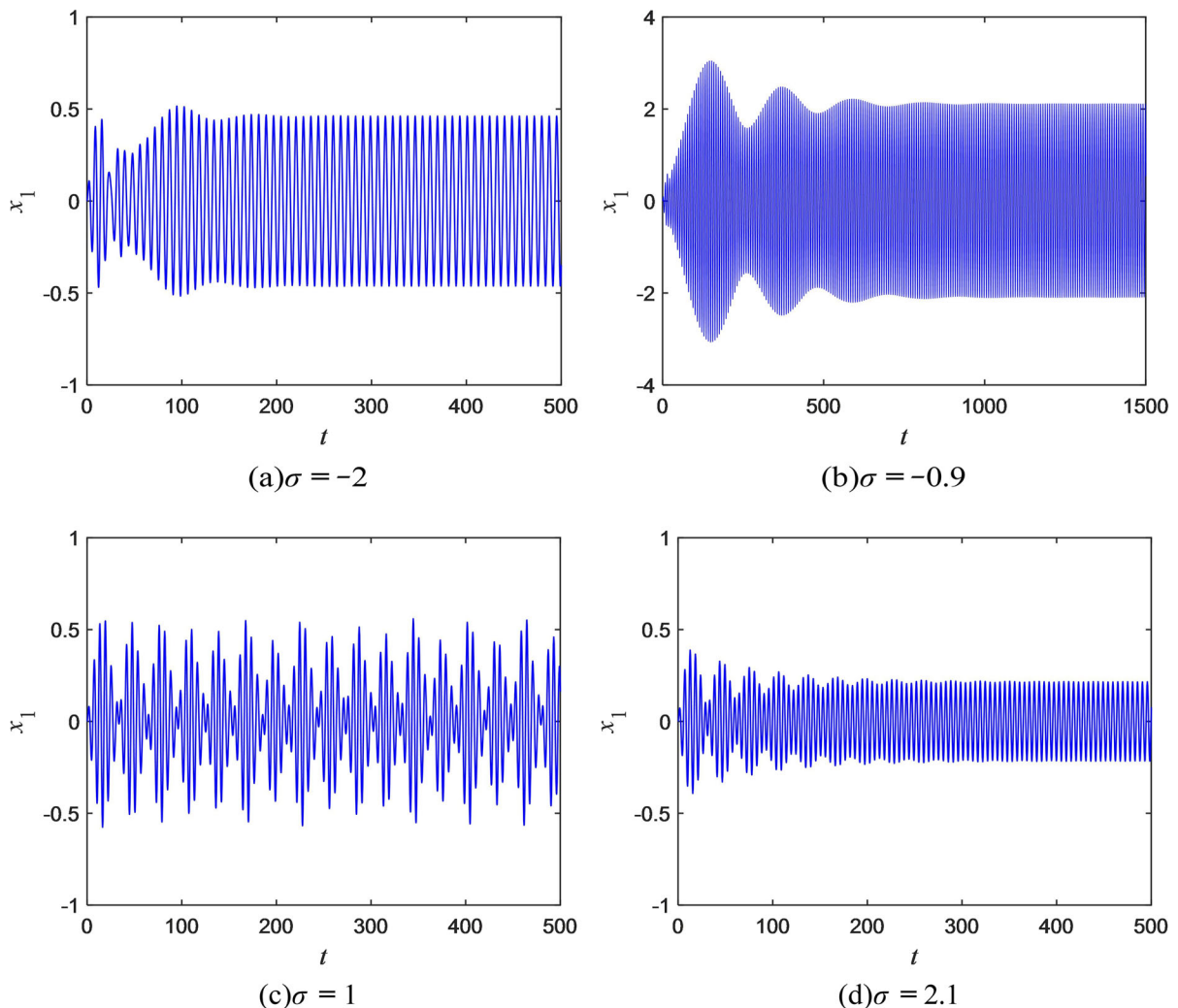


Fig. 11 Time response diagrams with σ change

energy of the main system with different damping NES under different impulsive excitation intensities are shown in Fig. 13.

In the figure above, L-NES represents linear damping NES, G-NES represents geometrically nonlinear damping NES, and LG-NES is a combined damping NES studied in this paper. As can be seen from Fig. 13, when the impulsive excitation intensity A remains constant, the dissipation time of E_1 with additional combined damping NES is the shortest, and the vibration attenuation of the main system is the fastest, indicating that the vibration reduction performance of combined damping NES is better than that of L-NES and G-NES. It is worth noting that with the increase of the impulsive excitation intensity A , the

vibration reduction performance of G-NES gradually exceeds that of L-NES. It shows that L-NES is suitable for use in environments with lower impulsive excitation intensity, and G-NES is suitable for use in environments with higher impulsive excitation intensity. But overall, the vibration reduction performance of combined damping NES is the best.

Next, analyze the effects of cubic stiffness coefficient k , linear damping coefficient λ_2 , and geometrically nonlinear damping coefficient λ_3 on the vibration reduction performance of combined damping NES. Firstly, study the vibration reduction performances under different k , and select the parameters as shown in the table below.

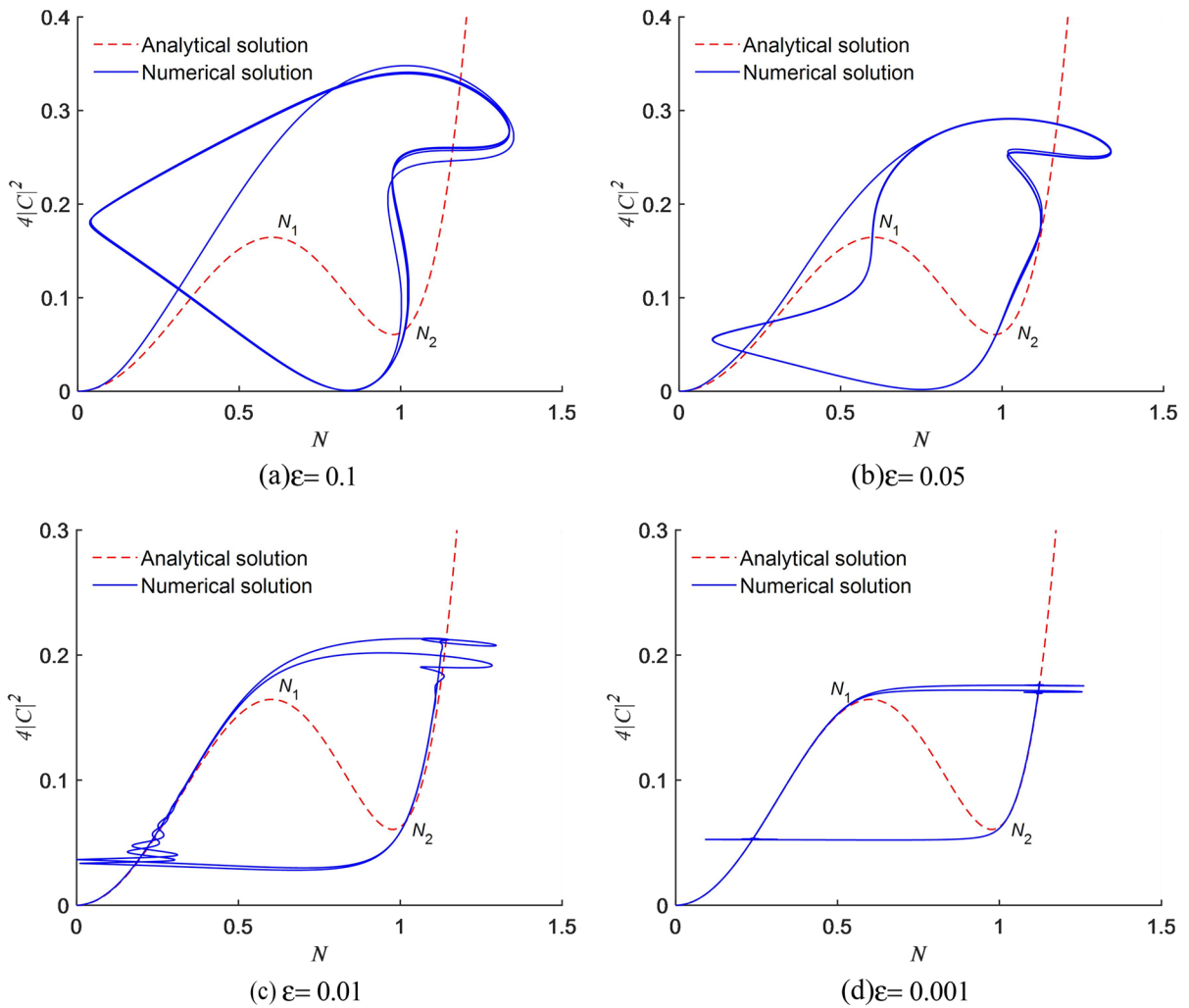


Fig. 12 Slow manifolds of the system response with ϵ change

According to the parameters selected in Table 1, the energy variation curves of the main system and combined damping NES when $A = 1$ m/s are drawn, as shown in Fig. 14.

As can be seen from Fig. 14a, when k is small, the energy transferred by the main system to combined damping NES is very low, and almost no energy transfer occurs. With the increase of k , the energy transferred by the main system to combined damping NES gradually increases, and the dissipation time of E_1 gradually becomes shorter, indicating that the vibration reduction performance of combined damping NES is gradually improved. However, when k is too large, as shown in Fig. 13d, the energy transferred by the main system to combined damping NES will

decrease, and the dissipation speed of E_1 will slow down, indicating that the vibration reduction performance of combined damping NES on the main system is deteriorating. Therefore, in order to make combined damping NES produce a good vibration suppression effect, it is necessary to select the appropriate k .

To verify the conclusion of Fig. 14, define the energy proportion η of the main system as follows

$$\eta = \frac{E_1}{E_0} \times 100\% = \frac{(x_1^2 + \dot{x}_1^2)}{A^2} \times 100\% \tag{49}$$

The energy proportion diagram of the main system under different k is drawn as shown in the figure below.

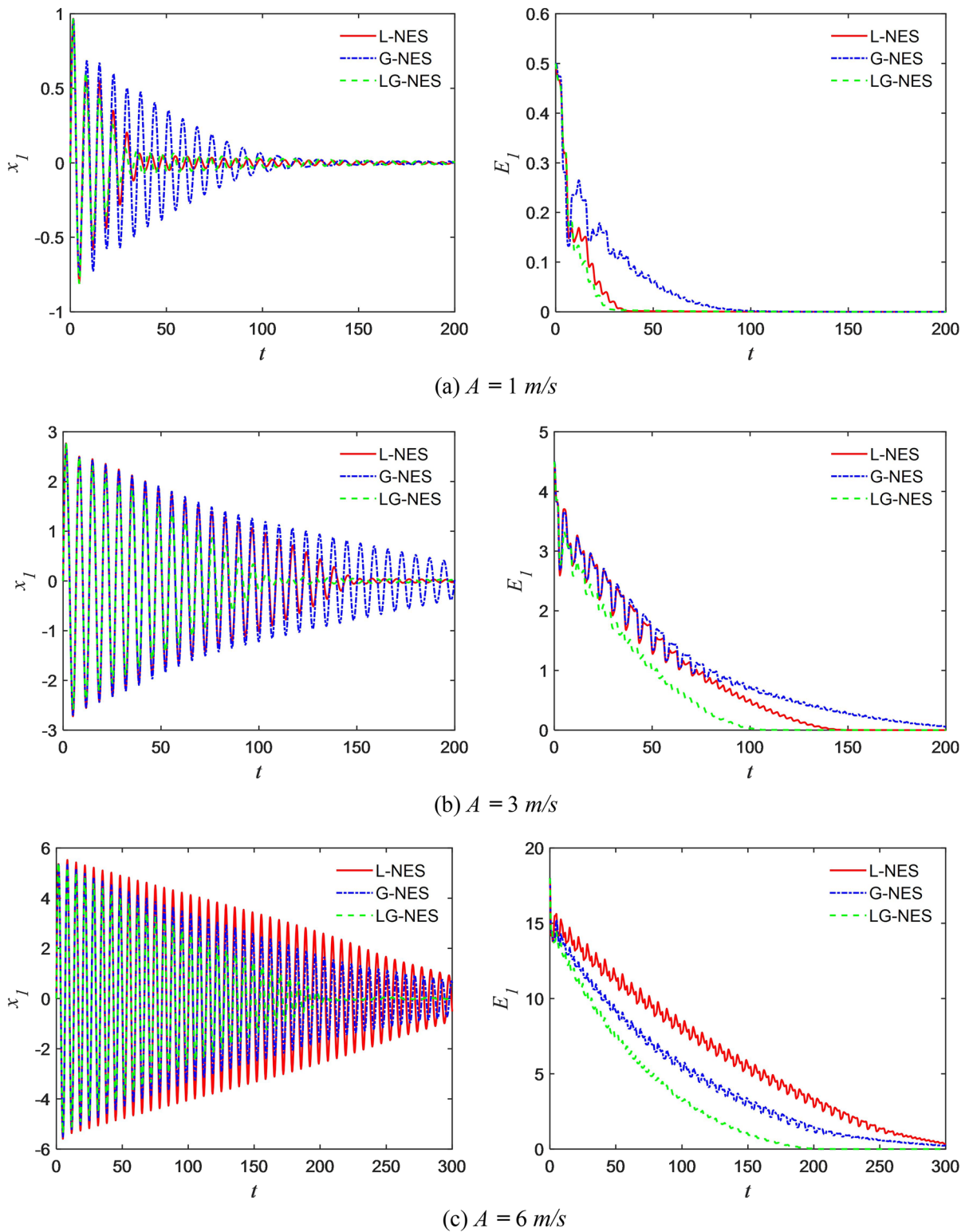


Fig. 13 The time response and energy of the main system with different damping NES under different impulsive excitation intensities

Table 1 Parameter value table

Serial number	k	λ_2	λ_3	ε
a	1/3	0.3	0.3	0.1
b	2/3	0.3	0.3	0.1
c	4/3	0.3	0.3	0.1
d	8/3	0.3	0.3	0.1

In Fig. 15, with the increase of k , the energy proportion curve of the main system shows a trend of first decreasing and then increasing, indicating that when k is too small or too large, the energy transmitted by the main system to combined damping NES is less, and the energy dissipation speed of the main system is slower. At this time, combined damping NES does not have a good vibration reduction effect.

Secondly, the effects of different linear damping coefficients λ_2 on the vibration reduction performance of combined damping NES are studied, and the parameters selection is shown in the table below.

According to the parameters selected in Table 2, the energy variation curves of the main system and combined damping NES when $A = 1$ m/s are drawn, as shown in the figure below.

As can be seen from Fig. 16a, when λ_2 is small, although the main system can transfer more energy to combined damping NES, combined damping NES will return energy to the main system, resulting in a longer energy dissipation time of the main system, which makes the main system unable to obtain good vibration reduction performance. With the increase of λ_2 , as shown in Fig. 15c, when the value is 0.3, the energy transmitted by the main system to combined damping NES is rarely returned to the main system by combined damping NES, and the energy of the main system will rapidly decrease. At this time, the main system can obtain a good vibration suppression effect. When the value of λ_2 is too large, as shown in Fig. 15d, the energy of the main system can hardly be transferred to combined damping NES, resulting in combined damping NES can not have a good vibration suppression effect.

Figure 17 plots the energy proportion of the main system under different linear damping coefficients.

As can be seen from Fig. 17, as λ_2 increases, the degree of rebound in the energy proportion curve of the main system decreases, and the dissipation time of

the energy proportion curve is shorter and shorter. This indicates that the energy returned to the main system by combined damping NES is gradually decreasing, and the vibration reduction effect of combined damping NES is getting better and better. When λ_2 is too large, the energy proportion curve changes more gently and the dissipation time becomes longer, indicating that the main system almost does not transfer energy to combined damping NES, and the combined damping NES does not provide a good reduction effect on the main system.

Finally, the effects of different geometrically nonlinear damping coefficients λ_3 on the vibration reduction performance of combined damping NES are studied, and the parameters selected are shown in the following table.

According to the parameters selected in Table 3, the energy variation curves of the main system and combined damping NES when the $A = 1$ m/s are drawn, as shown in Fig. 18.

In Fig. 18, as λ_3 increases, the energy variation curve of the main system becomes more gentle and the dissipation time becomes shorter, indicating that the energy returned by combined damping NES to the main system is less and less, and the vibration reduction effect of combined damping NES is getting better and better. However, when λ_3 is too large, as shown in Fig. 18d, the dissipation time of the main system energy increases, and the energy transmitted to combined damping NES decreases to a certain extent, indicating that the combined damping NES's vibration reduction effect has decreased. Therefore, it is necessary to select an appropriate λ_3 to make the main system obtain a good vibration reduction effect.

Figure 19 shows the energy proportion of the main system under different geometrically nonlinear damping coefficients.

It can be seen from Fig. 19 that the change of λ_3 has a small impact on the energy proportion curve of the main system. By enlarging the figure, it is found that the energy proportion curve of the main system becomes more gentle with the increase of λ_3 , indicating that the energy returned by combined damping NES to the main system gradually decreases. When λ_3 reaches 1.5, the dissipation rate of the energy proportion curve decreases to a certain extent. This figure can effectively validate the conclusion of Fig. 18.

In order to analyze the vibration reduction effect of combined damping NES under harmonic excitation,

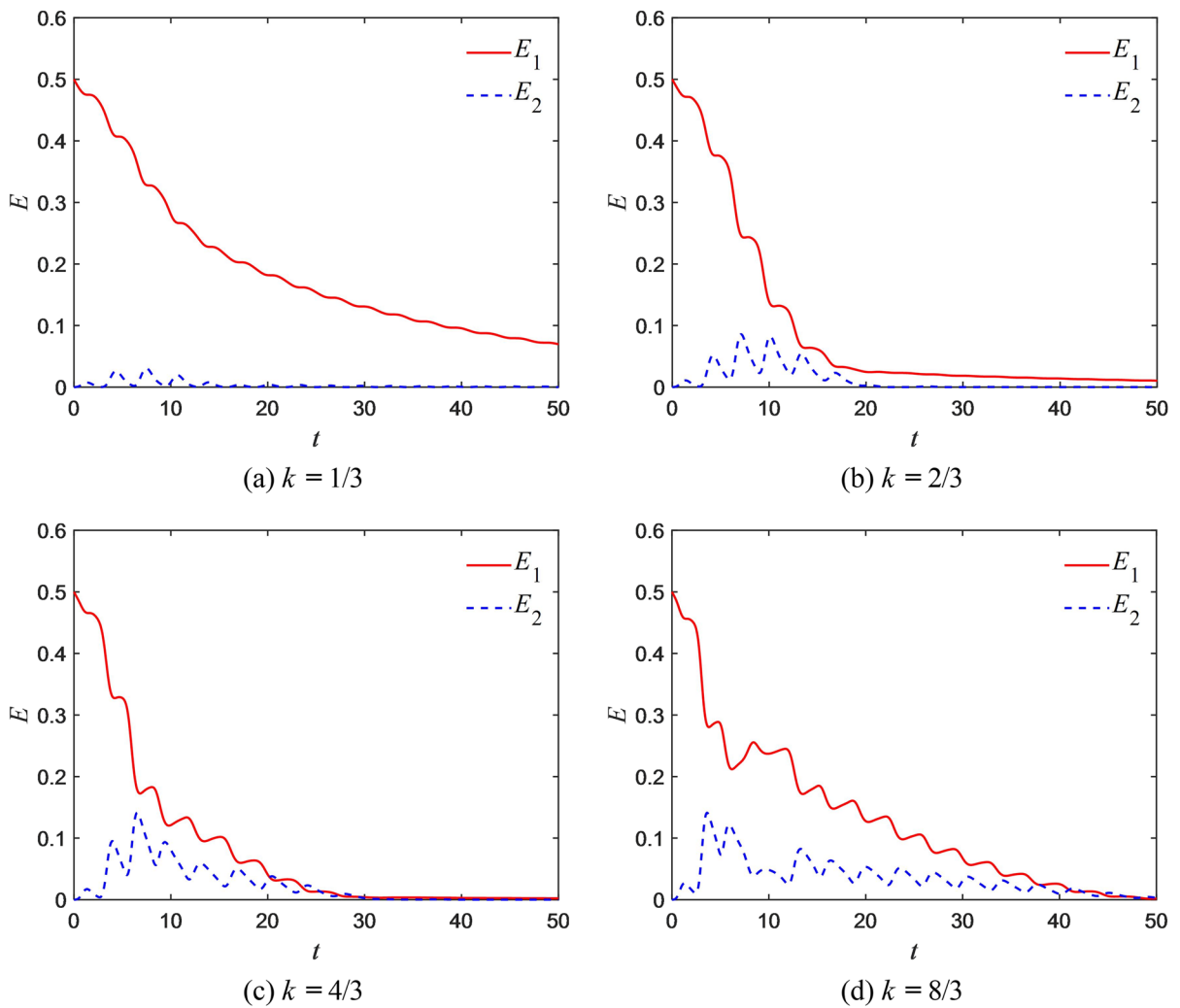


Fig. 14 E_1 and E_2 with different k

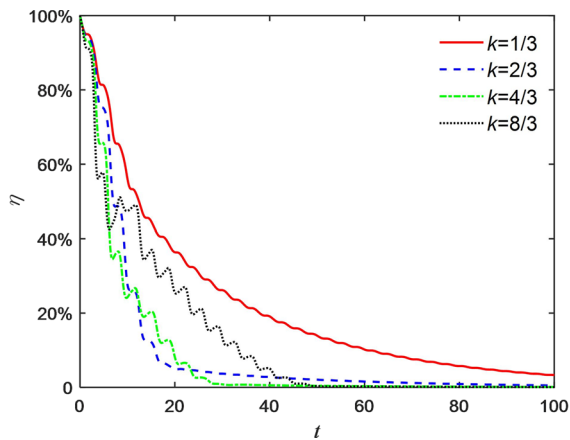


Fig. 15 Energy proportion of the main system with different k

Table 2 Parameter value table

Serial number	k	λ_2	λ_3	ε
a	4/3	0.01	0.3	0.1
b	4/3	0.1	0.3	0.1
c	4/3	0.3	0.3	0.1
d	4/3	0.8	0.3	0.1

the energy spectrum is used for comparative study in this part. According to Eq. (8), the average energy E_a of the main system can be expressed as:

$$E_a = \left\langle \frac{1}{2} \dot{x}_1^2 + \frac{1}{2} x_1^2 \right\rangle_t \tag{50}$$

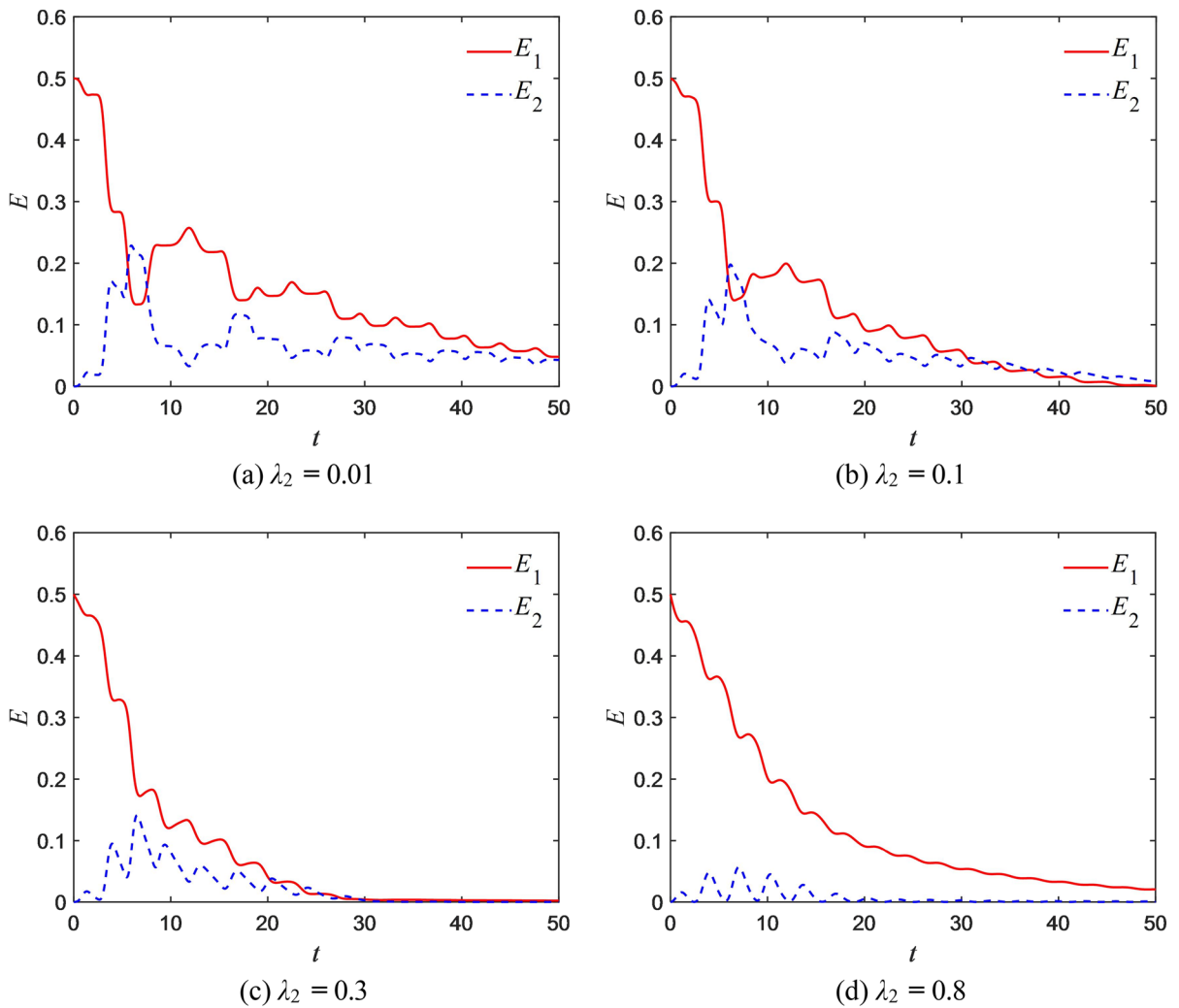


Fig. 16 E_1 and E_2 with different λ_2

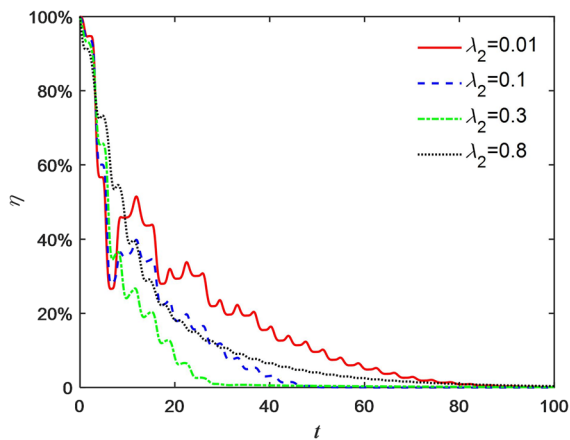


Fig. 17 Energy proportion of the main system with different λ_2

Table 3 Parameter value table

Serial number	k	λ_2	λ_3	ε
a	4/3	0.3	0.15	0.1
b	4/3	0.3	0.3	0.1
c	4/3	0.3	0.6	0.1
d	4/3	0.3	1.5	0.1

This equation means the average value of E_1 over time period t , and t must be greater than the period T of harmonic excitation. According to the above equation, when the value of E_a is the smallest, the

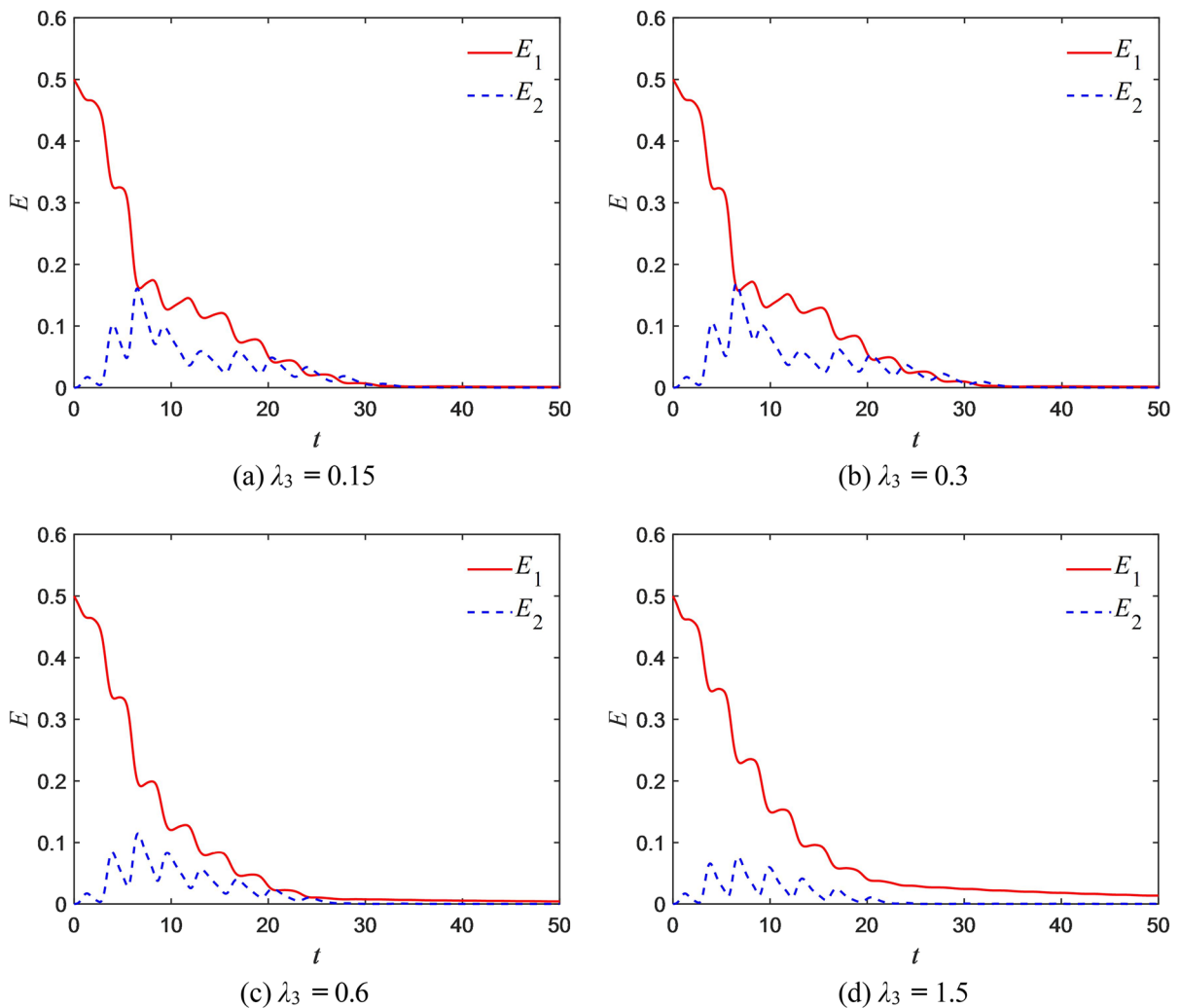


Fig. 18 E_1 and E_2 with different λ_3

combined damping NES has the best vibration suppression effect on the main system. For the convenience of comparing the vibration reduction effect of different damping NES, the parameter selection should be consistent with the literature results [19], and the values are: $t \in [2000, 3000]$, $f = 0.3$.

Next, analyze the influence of mass ratio ε , damping ratio λ_3/λ_2 and cubic stiffness coefficient k on the vibration reduction effect of combined damping NES. Firstly, draw the energy spectrum of the main system with different ε and λ_3/λ_2 as shown in the following figure.

As can be seen from Fig. 20, when ε and λ_3/λ_2 remain constant, the energy spectrum area of the main

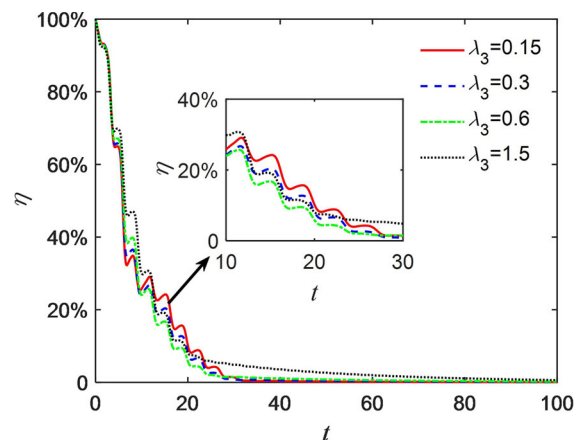


Fig. 19 Energy proportion of the main system with different λ_3

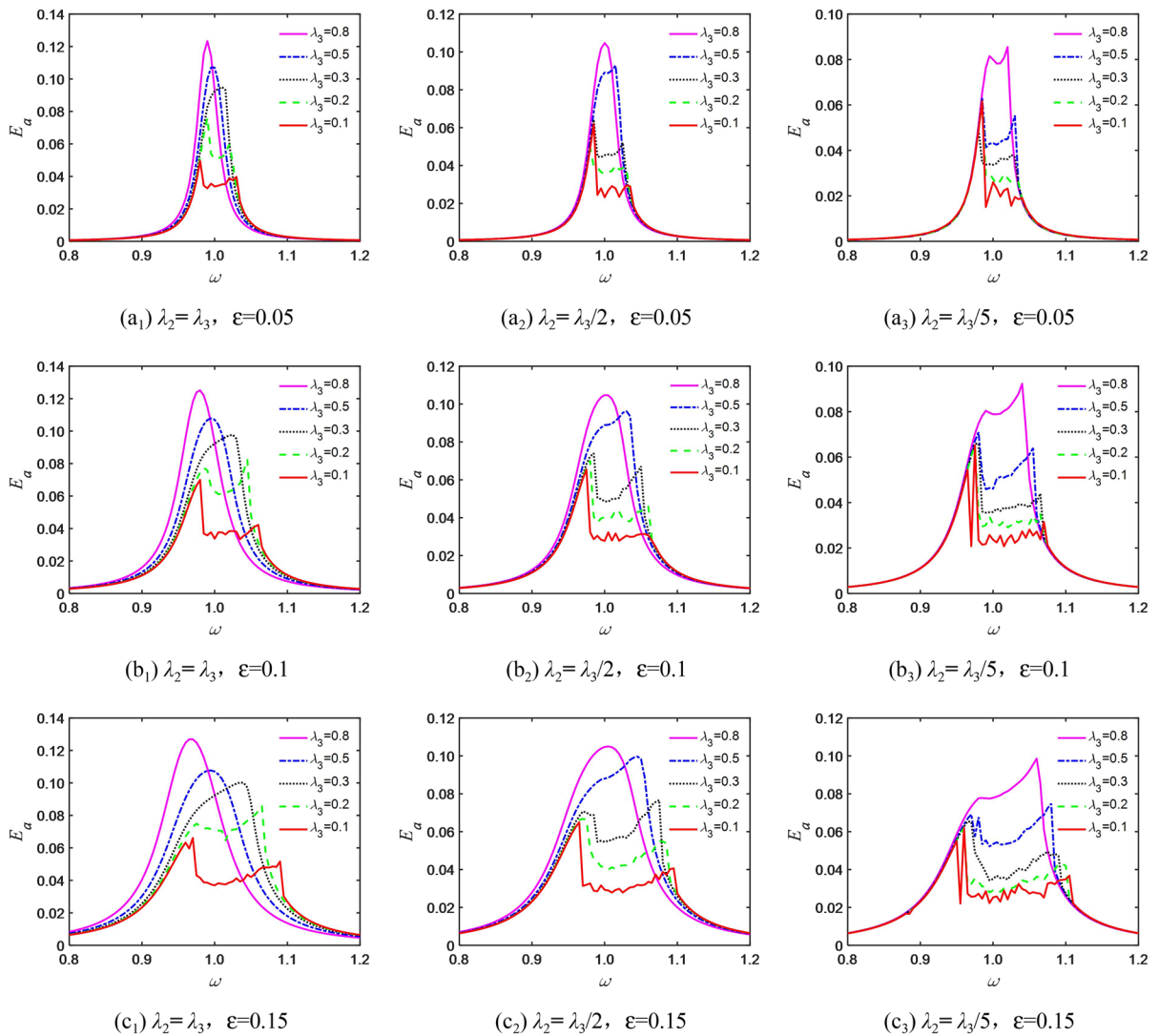


Fig. 20 Energy spectrum of the main system with ϵ and $\lambda_3 \lambda_2$ change

system does not decrease with the increase of the damping coefficient of combined damping NES, indicating that the vibration reduction effect of combined damping NES does not develop in a good direction. On the contrary, when the damping coefficient of combined damping NES is smaller, the energy spectrum area of the main system is smaller, and the vibration reduction effect of combined damping NES is better. As shown in Fig. 21, near the resonance frequency, when the value of λ_3 is 0.3, the SMR phenomenon occurs in the system, and the amplitude of the main system is greatly modulated. At this time, combined damping NES has a better vibration

reduction effect on the main system. When the value is 0.5, the system exhibits a weak modulation phenomenon, and the amplitude of the main system is subject to a certain degree of small modulation. When the value is 0.8, the main system presents a steady periodic response, which is not conducive to the vibration suppression of the main system. When ϵ remains constant, the energy spectrum area of the main system decreases with the increase of λ_3/λ_2 , indicating that the greater the difference between the linear damping coefficient and the geometrically damping coefficient, the better the vibration reduction effect of combined damping NES. When λ_3/λ_2

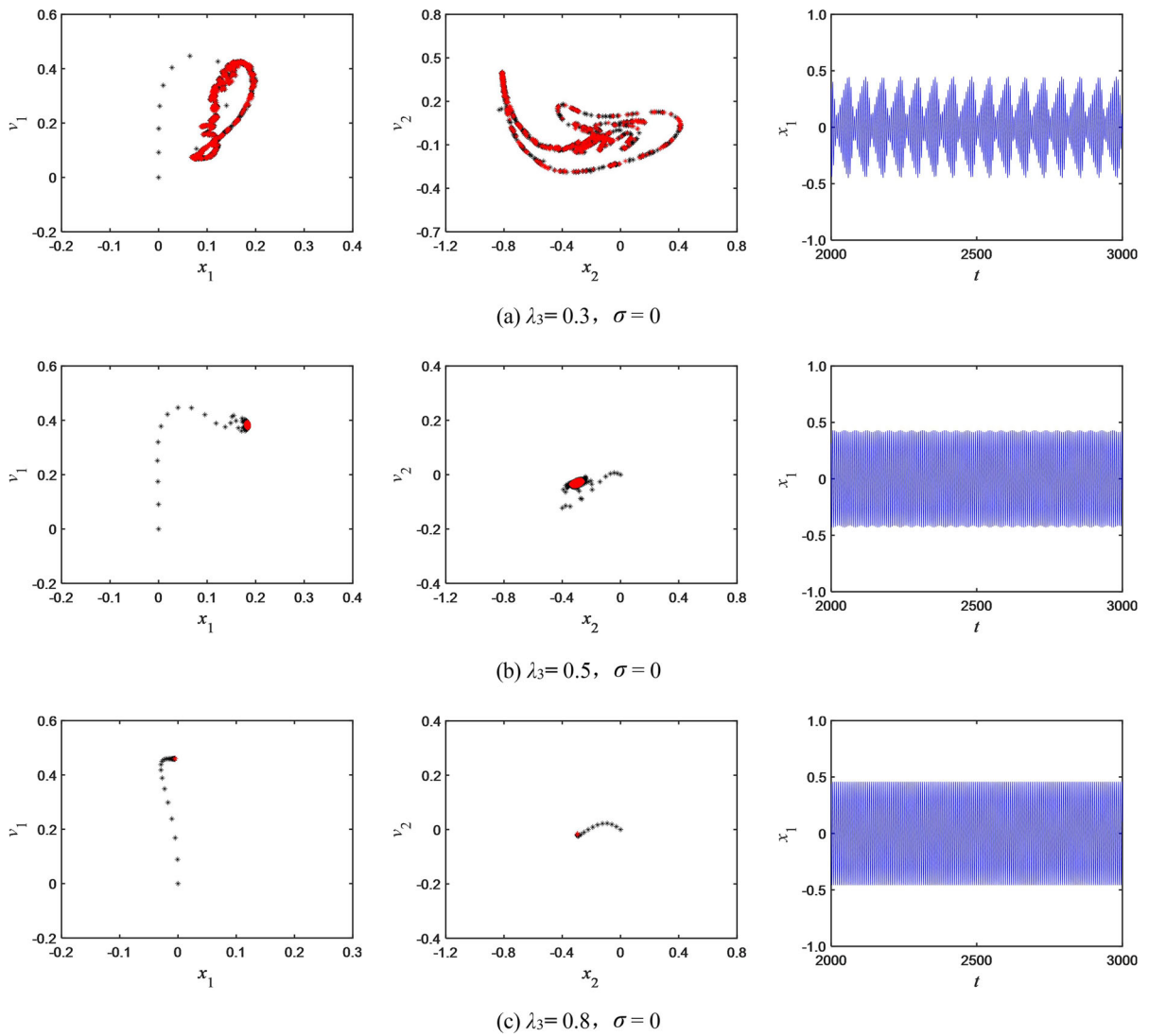


Fig. 21 Poincaré map and time response of different λ_3

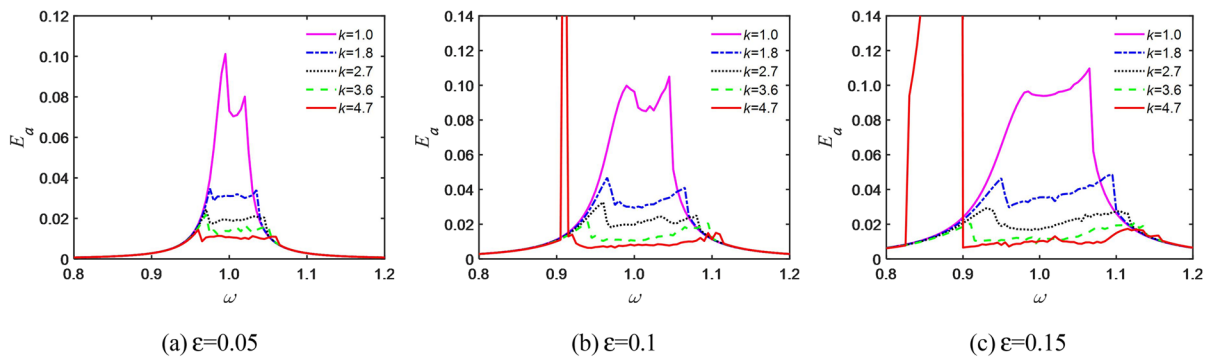


Fig. 22 Energy spectrum of the main system with ϵ and k change

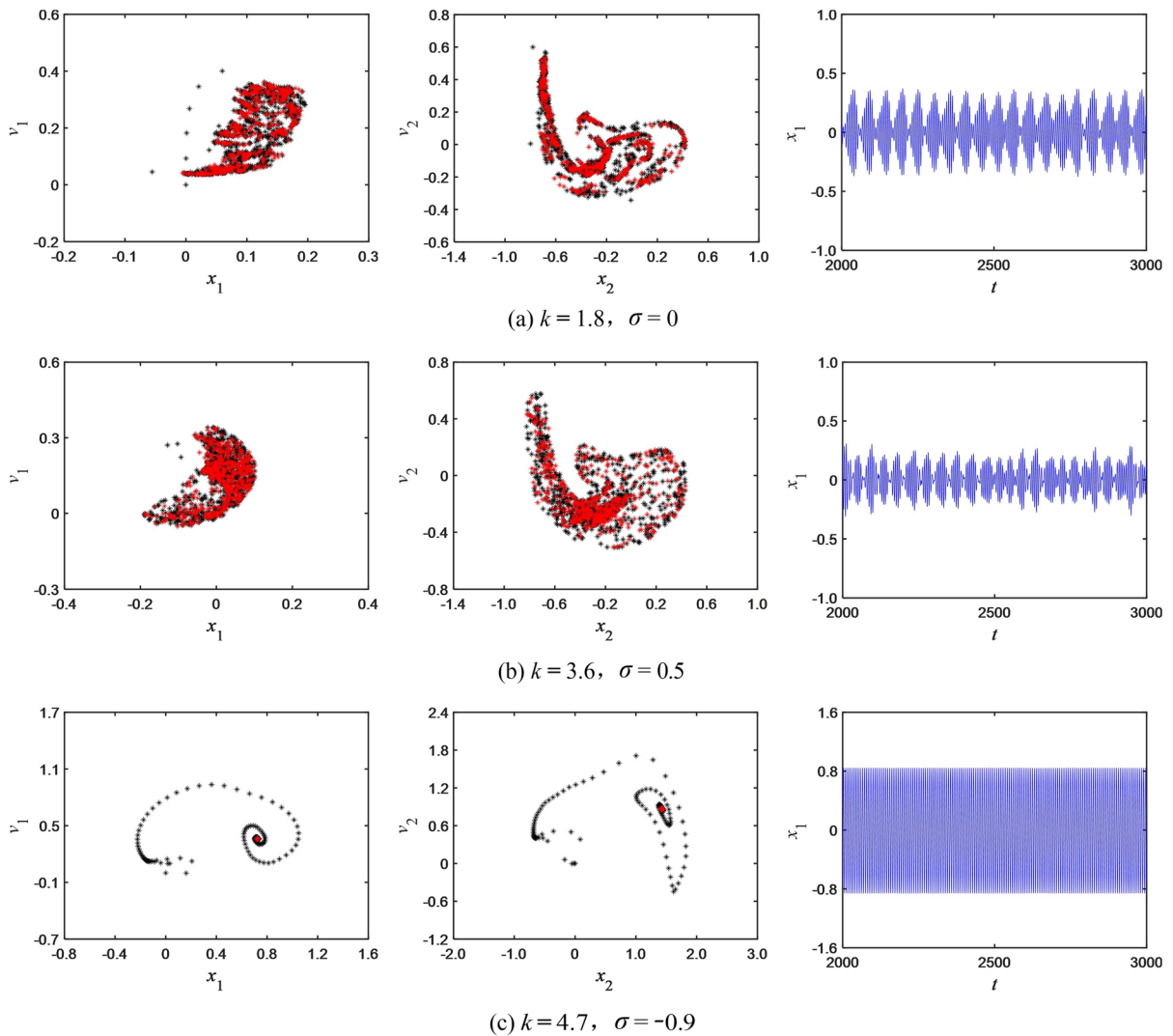


Fig. 23 Poincaré map and time response of different k and σ

remains constant, increasing ε will increase the energy spectrum area and bandwidth of the main system, which is not conducive to the vibration reduction of the main system by combined damping NES.

According to the previous analysis, the greater the λ_3/λ_2 , the better the vibration reduction effect of combined damping NES on the main system. Based on this, the damping ratio is taken as 5, and the energy spectrum of the main system with different ε and k is plotted as shown in the following figure.

According to Fig. 22, when ε remains constant, as k continues to increase, the energy spectrum area of the main system gradually decreases, and the bandwidth of vibration reduction continues to increase. At

this time, the main system will generate SMR phenomenon, and its amplitude will be greatly modulated, as shown in Fig. 23a and b. However, when k is too large, the energy spectrum of the main system will appear a resonance peak near the resonance frequency, causing the energy spectrum area to become very large. Drawing the Poincaré map and time response here, as shown in Fig. 23c, it can be found that the main system presents a steady periodic response without occurring SMR phenomenon, in which case the vibration reduction effect of combined damping NES is poor. The effect of ε change is the same as above, and increasing ε is not conducive to the vibration reduction effect of combined damping NES.

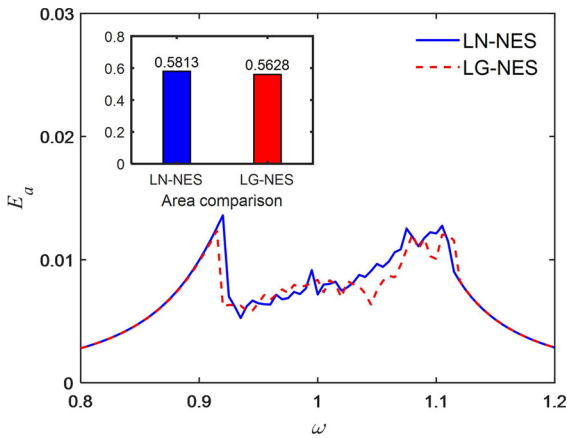


Fig. 24 Optimal energy spectrum comparison diagram

In summary, when designing combined damping NES parameters, it is necessary to select appropriately large stiffness coefficient k , smaller mass ratio ε and larger damping ratio λ_3/λ_2 to obtain smaller energy spectrum area and bandwidth, so as to achieve the optimal vibration reduction effect of combined damping NES on the main system.

In this paper, there are two standards to evaluate the vibration reduction effect of combined damping NES, the main standard is the energy spectrum area of the main system, and the secondary standard is the peak value at each position of the energy spectrum. According to these two standards, the parameters of combined damping NES are optimized. In the optimization process, considering that the energy spectrum of the main system is mainly concentrated near the resonance frequency, the frequency range is selected as $\omega = [0.8, 1.2]$, the weight allocation ratio is 80% of the energy spectrum area and 20% of the peak variance of the energy spectrum. After optimization, the optimal parameters are obtained as: $\lambda_2 = 0.05$, $\lambda_3 = 1.7$, $k = 5.31$, and compared with NES studied in the literature [40], the comparison diagram of the optimal energy spectrum is shown in Fig. 24.

In the figure, LN-NES represents NES with linear damping and cubic damping, while LG-NES represents NES with combined damping studied in this paper. As shown in Fig. 23, the energy spectrum area of the main system of LG-NES is smaller than that of LN-NES, and the peak in most positions is lower than that of LN-NES. Therefore, it can be concluded that the vibration reduction effect of LG-NES is better than that of LN-NES.

4.2 Amplitude-frequency response analysis

This section studies the vibration reduction effect of combined damping NES on the main system from the perspective of analytical solution, and analyzes the influence of NES parameters on the vibration reduction performance by using the amplitude-frequency response curve. Introduce a new complex variable to Eq. (9).

$$\gamma_1 e^{i\omega t} = \dot{u} + i\omega u, \quad \gamma_2 e^{i\omega t} = \dot{v} + i\omega v \tag{51}$$

Then Eq. (9) is transformed into

$$\begin{cases} \dot{\gamma}_1 + i \frac{[-1 + (1 + \varepsilon)\omega^2]\gamma_1 - \varepsilon\gamma_2}{2(1 + \varepsilon)\omega} = \frac{\varepsilon f}{2} \\ \dot{\gamma}_2 + \frac{1}{2}(i\omega + \lambda_2 + \varepsilon\lambda_2)\gamma_2 + \frac{1 + \varepsilon}{8\omega^2} \lambda_3 |\gamma_2|^2 \gamma_2 \\ \quad - \frac{3ik(1 + \varepsilon)}{8} |\gamma_2|^2 \gamma_2 - \frac{i(\gamma_1 + \varepsilon\gamma_2)}{2(1 + \varepsilon)\omega} = \frac{\varepsilon f}{2} \end{cases} \tag{52}$$

In order to obtain the steady solution of the system, letting $\dot{\gamma}_1 = \dot{\gamma}_2 = 0$, and perform the following transformations on γ_1 and γ_2 .

$$\gamma_1 = \beta_1 e^{i\alpha_1}, \quad \gamma_2 = \beta_2 e^{i\alpha_2} \tag{53}$$

By substituting Eqs. (53) into (52), we can yield

$$\begin{cases} \frac{[-1 + (1 + \varepsilon)\omega^2]\beta_1 \sin \alpha_1 - \varepsilon\beta_2 \sin \alpha_2 + \varepsilon f(1 + \varepsilon)\omega}{2(1 + \varepsilon)\omega} = 0 \\ \frac{[-1 + (1 + \varepsilon)\omega^2]\beta_1 \cos \alpha_1 - \varepsilon\beta_2 \cos \alpha_2}{2(1 + \varepsilon)\omega} = 0 \\ \frac{1}{8} \left[-4\varepsilon f + \frac{(1 + \varepsilon)\lambda_3}{\omega^2} \beta_2^3 \cos \alpha_2 + \frac{3k(1 + \varepsilon)}{\omega^3} \beta_2^3 \sin \alpha_2 \right. \\ \quad \left. + \frac{4\beta_1 \sin \alpha_1}{(1 + \varepsilon)\omega} \right] \\ \quad + \frac{(1 + \varepsilon)^2 \lambda_2 \omega \beta_2 \cos \alpha_2 + [\varepsilon - (1 + \varepsilon)\omega^2]\beta_2 \sin \alpha_2}{2(1 + \varepsilon)\omega} = 0 \\ \frac{1}{8} \left[\frac{(1 + \varepsilon)\lambda_3}{\omega^2} \beta_2^3 \sin \alpha_2 - \frac{3k(1 + \varepsilon)}{\omega^3} \beta_2^3 \cos \alpha_2 - \frac{4\beta_1 \cos \alpha_1}{(1 + \varepsilon)\omega} \right] \\ \quad + \frac{(1 + \varepsilon)^2 \lambda_2 \omega \beta_2 \sin \alpha_2 + [(1 + \varepsilon)\omega^2 - \varepsilon]\beta_2 \cos \alpha_2}{2(1 + \varepsilon)\omega} = 0 \end{cases} \tag{54}$$

According to the paper studied by Fang et al. [41], it can be obtained

$$u(t) \approx \frac{\beta_1}{\omega} \sin(\omega t + \alpha_1), \quad v(t) \approx \frac{\beta_2}{\omega} \sin(\omega t + \alpha_2) \tag{55}$$

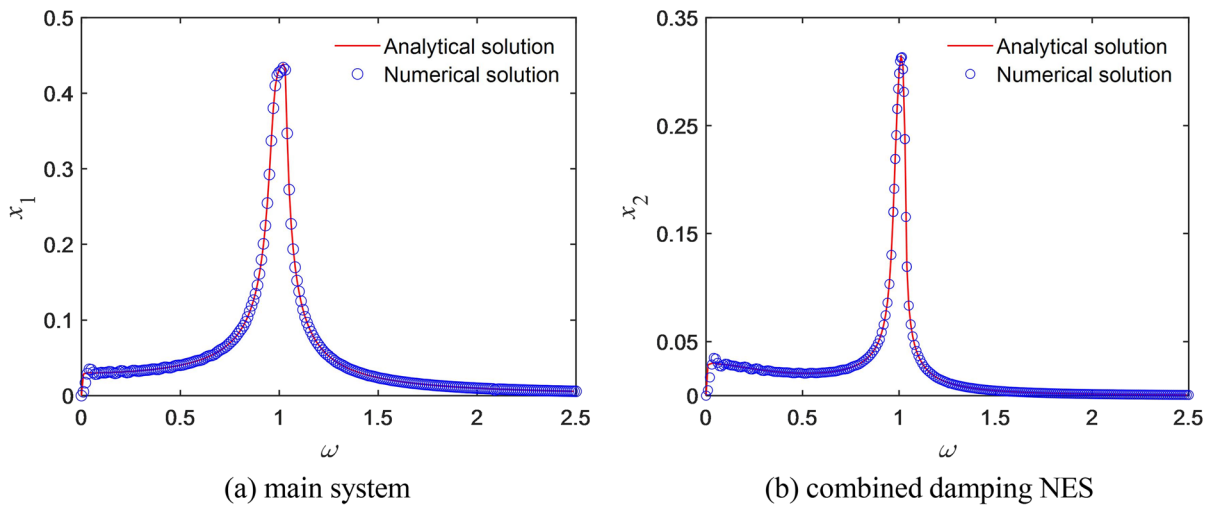


Fig. 25 Comparison of the amplitude-frequency response curves

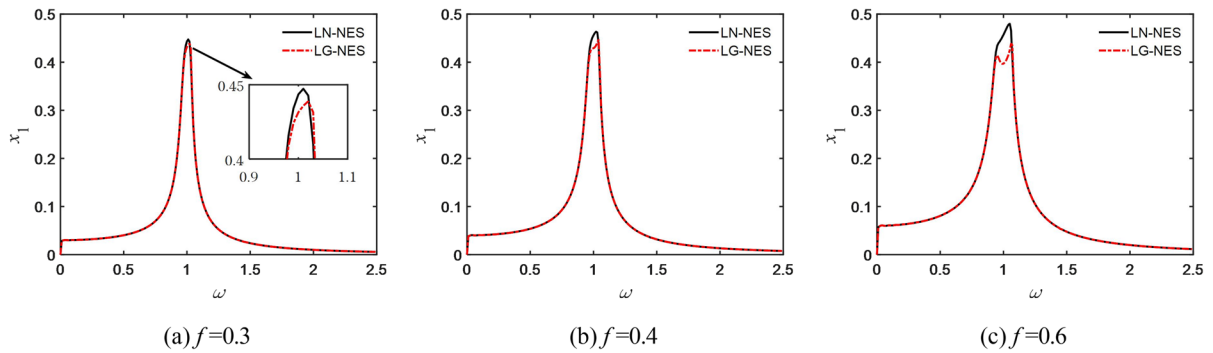


Fig. 26 Amplitude-frequency response curves of different NES at different f

The steady-state response of the system is obtained as

$$\begin{cases} x_1(t) \approx \frac{1}{1 + \varepsilon} \left[\frac{\beta_1}{\omega} \sin(\omega t + \alpha_1) + \varepsilon \frac{\beta_2}{\omega} \sin(\omega t + \alpha_2) \right] \\ x_2(t) \approx \frac{1}{1 + \varepsilon} \left[\frac{\beta_1}{\omega} \sin(\omega t + \alpha_1) - \frac{\beta_2}{\omega} \sin(\omega t + \alpha_2) \right] \end{cases} \quad (56)$$

Solve Eq. (54) and bring the results into Eq. (56) to obtain the analytical solution of the response amplitude. Meanwhile, using the Runge Kutta method to solve Eq. (8) to obtain the numerical solution of the response amplitude. Draw the amplitude-frequency response curves of the main system and combined damping NES, as shown in Fig. 25.

It can be seen from Fig. 25 that the analytical solution and the numerical solution agree well, which verifies the correctness of the complex variable average method to solve the response amplitude.

Figure 26 shows the amplitude-frequency response curves of the main system for different NES under different external excitation amplitudes. From Fig. 26, it can be seen that when the two NES selected the same parameters, the resonance amplitude of LG-NES is lower than that of LN-NES. Moreover, when the external excitation amplitude increases, the difference in resonance amplitude between LG-NES and LN-NES is more significant, indicating that the vibration reduction effect of LG-NES is better than that of LN-NES. Moreover, when the external excitation amplitude is larger, the vibration reduction advantage of LG-NES is more obvious.

Next, analyze the influence of NES parameter changes on the vibration reduction performance of combined damping NES. Firstly, analyze the influence of mass ratio ε , damping ratio λ_3/λ_2 and damping coefficient on the vibration reduction effect.

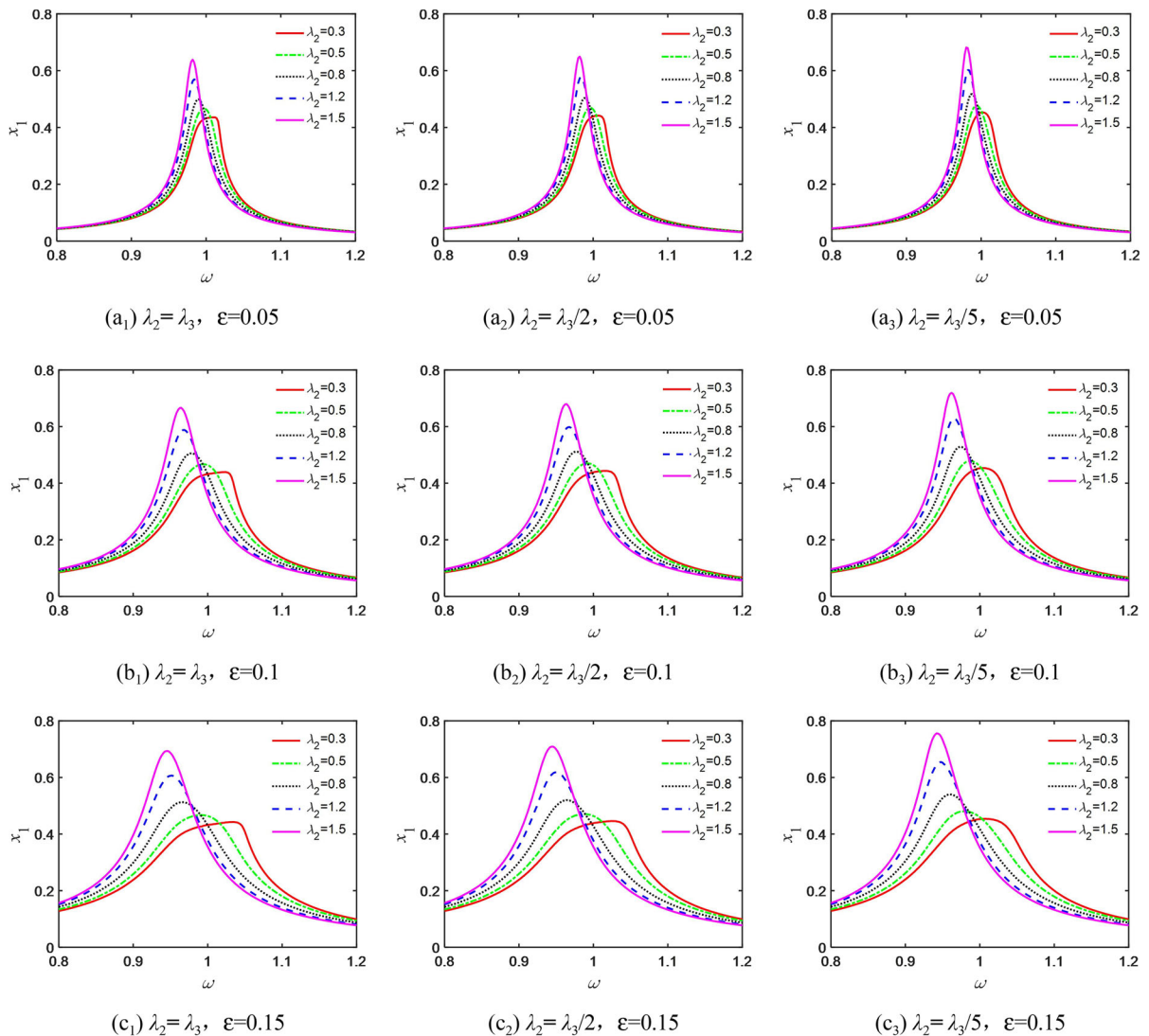


Fig. 27 Amplitude-frequency response curves with ε and λ_3/λ_2 change

Parameters selected as: $k = 4/3$, $f = 0.3$ [31], and draw the amplitude-frequency response curves of the main system with different ε and λ_3/λ_2 as shown in the following figure.

As can be seen from Fig. 27, when ε and λ_3/λ_2 remain constant, the steady-state response amplitude near the resonance frequency of the main system increases with the increase of the damping coefficient, which indicates that the vibration reduction performance of combined damping NES gradually decreases with the increase of the damping coefficient. Therefore, when choosing the damping coefficient, we should choose a smaller damping coefficient to make

the main system get a good vibration reduction effect. When the damping coefficient and ε remain constant, with the increase of λ_3/λ_2 , although the steady-state response amplitude of the main system near the resonance frequency increases to a certain extent, the frequency band of resonance becomes narrower. Therefore, when selecting the damping ratio, it is necessary to choose an appropriately large damping ratio. When the damping coefficient and λ_3/λ_2 remain constant, both the resonant frequency band and steady-state response amplitude of the main system increase with the increase of ε , indicating that the vibration reduction performance of combined damping NES is

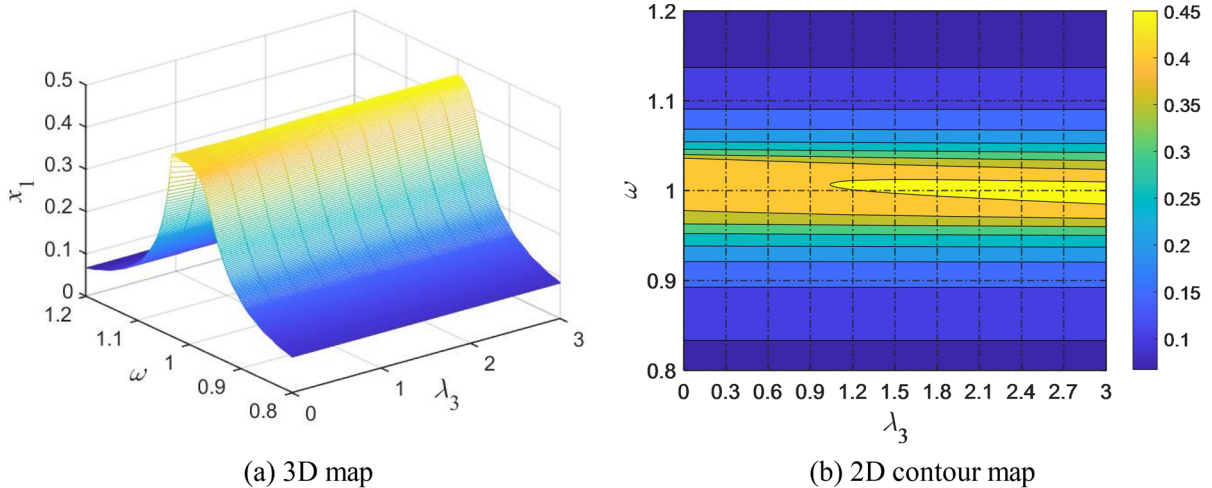


Fig. 28 Amplitude-frequency response curves with λ_3 change

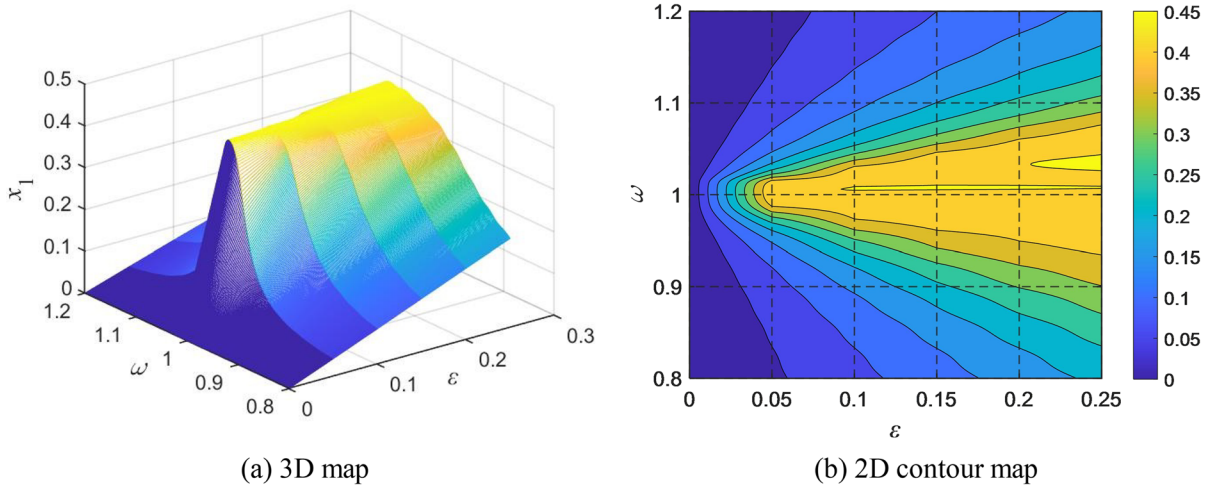


Fig. 29 Amplitude-frequency response curves with ϵ change

gradually declining. Therefore, it is necessary to choose a smaller ϵ .

In order to further study the optimal range of the above parameters, 3D and 2D contour maps with different λ_3/λ_2 and ϵ are drawn, as shown in Figs. 28 and 29. The parameter selection is the same as above.

As can be seen from Fig. 28, when λ_3/λ_2 is about 3.5, the amplitude-frequency response curve of the main system not only does not show a high steady-state response amplitude, but also has a narrow resonance frequency band. Therefore, in the subsequent analysis, the damping ratio is selected as 3.5.

Figure 29 shows the amplitude-frequency response curves of the main system with different ϵ .

It can be observed from Fig. 29 that when ϵ is 0.21, there is obviously a large response amplitude near the main resonance frequency, which is not conducive to the vibration reduction of the main system. Meanwhile, it is also found that the larger ϵ , the wider the frequency range of the system resonance. Therefore, a smaller ϵ should be selected to obtain a good vibration reduction effect for the main system.

According to the conclusions of Figs. 28 and 29, the damping ratio λ_3/λ_2 is 3.5 and the mass ratio ϵ is 0.1. The amplitude-frequency response curves of the main

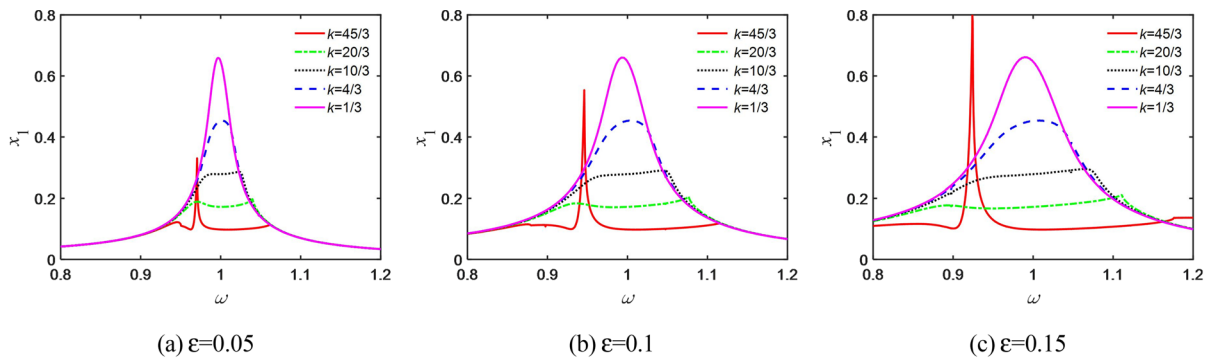


Fig. 30 Amplitude-frequency response curves with ε and k change

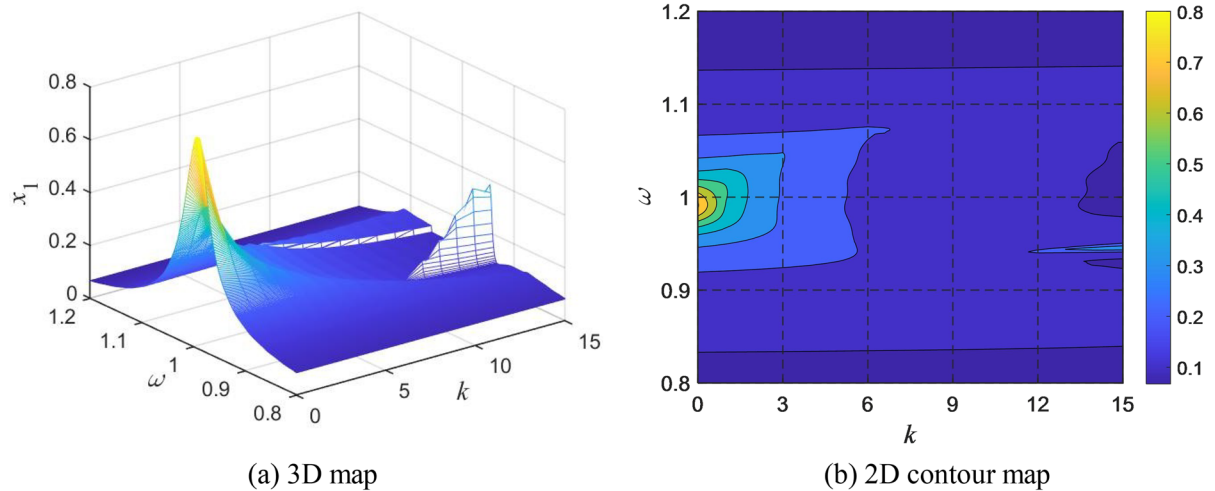


Fig. 31 Amplitude-frequency response curves with k change

system with different ε and stiffness coefficient k are drawn, as shown in Fig. 30:

It can be seen from Fig. 30 that the influence of ε is the same as above, and it will not be repeated here. When ε is unchanged, the steady-state response amplitude of the main system gradually decreases with the increase of k . However, when k is too large, a resonance peak will appear near the resonance frequency, which is not conducive to LN-NES to reduce the vibration of the main system.

In order to further determine the range of k , 3D and 2D contour maps of different k are drawn in Fig. 31. According to the figure below, when the value of k is greater than 6.9, the steady-state response amplitude of the main system is relatively small, basically at the same height. When the value exceeds 11.8, a resonance peak begins to appear near the resonance frequency, which is not conducive to the system

vibration reduction. Therefore, under this set of parameters, the value range of k is (6.9, 11.8).

5 Conclusion

In this study, the bifurcation characteristics and strongly modulated response of the combined damping NES are studied, and the vibration suppression effect of the combined damping NES under different excitation is analyzed.

For the study of bifurcation characteristics, by analyzing the influence of NES parameters on SN bifurcation and Hopf bifurcation, it is found that the smaller the linear damping coefficient λ_2 , the larger the mass ratio ε and the detuning parameter σ , the larger the area of the system to obtain the three unstable fixed points. Meanwhile, by analyzing the

influence of excitation amplitude and excitation frequency on the system response amplitude. It is found that the system is unstable only in the vicinity of $f = 3.2$ and $\sigma = 0$.

For the study of strongly modulated response, by analyzing the slow invariant manifold and phase portrait of the system, it is found that continuous jumps can provide the possibility for the system to have SMR phenomenon. Then, the slow manifold is used to analyze the detuning parameter range of SMR in the system from a numerical perspective, and it is concluded that the detuning parameter interval for the occurrence of SMR in the system is $[-0.19, 1.52]$.

For the analysis of vibration reduction performance, On the one hand, the damping effect of the combined damping NES under pulse excitation and harmonic excitation is studied. By analyzing the amplitude and energy spectrum of the main system, it is found that the vibration suppression effect of the combined damping NES is better than that of the linear damping NES and the geometrically nonlinear damping NES. On the other hand, the parameters of the system are optimized by the amplitude-frequency response and the maximum amplitude, and the optimal parameters of the combined damping NES are pointed out.

Author Contributions All authors contributed to the study conception and design. Material preparation and analysis were performed by [Qi xing-ke], [Zhang jian-chao] and [Wang jun]. The first draft of the manuscript was written by [Qi xing-ke] and all authors commented on previous versions of the manuscript. All authors read and approved the final manuscript.

Funding This work was supported by the National Natural Science Foundation of China through Grant No. 11872256.

Data Availability The data used in this article can be found in the references.

Declarations

Competing interests I declare that the authors have no competing interests as defined by Springer, or other interests that might be perceived to influence the results and/or discussion reported in this paper.

Ethical approval Not.

Human and animal ethics Not applicable.

References

1. Saeed, A.S., AbdulNasar, R., AL-Shudeifat, M.A.: A review on nonlinear energy sinks: designs, analysis and applications of impact and rotary types. *Nonlinear Dyn.Dyn.* **111**(1), 1–37 (2023)
2. Ding, H., Chen, L.Q.: Designs, analysis, and applications of nonlinear energy sinks. *Nonlinear Dyn.Dyn.* **100**(4), 3061–3107 (2020)
3. Housner, G.W., Bergman, L.A., Caughey, T.K., et al.: Structural control: past, present, and future. *J. Eng. Mech.* **123**(9), 897–971 (1997)
4. Brennan, M.J.: Vibration control using a tunable vibration neutralizer. *Proc. Inst. Mech. Eng. C J. Mech. Eng. Sci.* **211**(2), 91–108 (1997)
5. Thompson, D.J.: A continuous damped vibration absorber to reduce broad-band wave propagation in beams. *J. Sound Vib.Vib.* **311**(3–5), 824–842 (2008)
6. Balaji, P.S., Karthik, S.K.: Applications of nonlinearity in passive vibration control: a review. *J. Vib. Eng. Technol.* **9**, 183–213 (2021)
7. Lu, Z., Wang, Z., Zhou, Y., et al.: Nonlinear dissipative devices in structural vibration control: a review. *J. Sound Vib.Vib.* **423**, 18–49 (2018)
8. Tehrani, G.G., Dardel, M., Pashaei, M.H.: Passive vibration absorbers for vibration reduction in the multi-bladed rotor with rotor and stator contact. *Acta Mech. Mech.* **231**, 597–623 (2020)
9. Roberson, R.E.: Synthesis of a nonlinear dynamic vibration absorber. *J. Franklin Inst.* **254**(3), 205–220 (1952)
10. Charlemagne, S., Lamarque, C.H., Savadkoobi, A.T.: Dynamics and energy exchanges between a linear oscillator and a nonlinear absorber with local and global potentials. *J. Sound Vib.Vib.* **376**, 33–47 (2016)
11. Sarmeili, M., Ashtiani, H.R.R., Rabiee, A.H.: Nonlinear energy sinks with nonlinear control strategies in fluid-structure simulations framework for passive and active FIV control of sprung cylinders. *Commun. Nonlinear Sci. Numer. Simul.. Nonlinear Sci. Numer. Simul.* **97**, 105725 (2021)
12. Wang, J., Wang, B., Wierschem, N.E., et al.: Dynamic analysis of track nonlinear energy sinks subjected to simple and stochastic excitations. *Earthquake Eng. Struct. Dynam.Struct. Dynam.* **49**(9), 863–883 (2020)
13. Li, H., Li, A., Kong, X.: Design criteria of bistable nonlinear energy sink in steady-state dynamics of beams and plates. *Nonlinear Dyn.Dyn.* **103**(2), 1475–1497 (2021)
14. Zang, J., Cao, R.Q., Zhang, Y.W.: Steady-state response of a viscoelastic beam with asymmetric elastic supports coupled to a lever-type nonlinear energy sink. *Nonlinear Dyn.Dyn.* **105**, 1327–1341 (2021)
15. Chen, J.E., Sun, M., Hu, W.H., et al.: Performance of non-smooth nonlinear energy sink with descending stiffness. *Nonlinear Dyn.Dyn.* **100**, 255–267 (2020)
16. Geng, X.F., Ding, H., Mao, X.Y., et al.: Nonlinear energy sink with limited vibration amplitude. *Mech. Syst. Signal Process.* **156**, 107625 (2021)

17. Wang, G.X., Ding, H., Chen, L.Q.: Performance evaluation and design criterion of a nonlinear energy sink. *Mech. Syst. Signal Process.* **169**, 108770 (2022)
18. Yang, T., Hou, S., Qin, Z.H., et al.: A dynamic reconfigurable nonlinear energy sink. *J. Sound Vib.* **494**, 115629 (2021)
19. Zhang, Y., Kong, X., Yue, C.: Vibration analysis of a new nonlinear energy sink under impulsive load and harmonic excitation. *Commun. Nonlinear Sci. Numer. Simul. Nonlinear Sci. Numer. Simul.* **116**, 106837 (2023)
20. Wang, J., Wierschem, N., Spencer, B.F., Jr., et al.: Experimental study of track nonlinear energy sinks for dynamic response reduction. *Eng. Struct.* **94**, 9–15 (2015)
21. Remick, K., Quinn, D.D., McFarland, D.M., et al.: High-frequency vibration energy harvesting from impulsive excitation utilizing intentional dynamic instability caused by strong nonlinearity. *J. Sound Vib.* **370**, 259–279 (2016)
22. Remick, K., Quinn, D.D., McFarland, D.M., et al.: High-frequency vibration energy harvesting from repeated impulsive forcing utilizing intentional dynamic instability caused by strong nonlinearity. *J. Intell. Mater. Syst. Struct. Intell. Mater. Syst. Struct.* **28**(4), 468–487 (2017)
23. Gendelman, O.V., Gourdon, E., Lamarque, C.H.: Quasiperiodic energy pumping in coupled oscillators under periodic forcing. *J. Sound Vib.* **294**(4–5), 651–662 (2006)
24. Gendelman, O.V., Starosvetsky, Y.: Quasi-periodic response regimes of linear oscillator coupled to nonlinear energy sink under periodic forcing. *J. Appl. Mech.* **74**(2), 325–331 (2007). <https://doi.org/10.1115/1.2198546>
25. Gendelman, O.V., Starosvetsky, Y., Feldman, M.: Attractors of harmonically forced linear oscillator with attached nonlinear energy sink I: description of response regimes. *Nonlinear Dyn.* **51**, 31–46 (2008)
26. Starosvetsky, Y., Gendelman, O.V.: Bifurcations of attractors in forced system with nonlinear energy sink: the effect of mass asymmetry. *Nonlinear Dyn.* **59**, 711–731 (2010)
27. Starosvetsky, Y., Gendelman, O.V.: Vibration absorption in systems with a nonlinear energy sink: nonlinear damping. *J. Sound Vib.* **324**(3–5), 916–939 (2009)
28. Starosvetsky, Y., Gendelman, O.V.: Response regimes in forced system with non-linear energy sink: quasi-periodic and random forcing. *Nonlinear Dyn.* **64**, 177–195 (2011)
29. Kong, X., Li, H., Wu, C.: Dynamics of 1-dof and 2-dof energy sink with geometrically nonlinear damping: application to vibration suppression. *Nonlinear Dyn.* **91**, 733–754 (2018)
30. Zhang, Y., Kong, X., Yue, C., et al.: Dynamic analysis of 1-dof and 2-dof nonlinear energy sink with geometrically nonlinear damping and combined stiffness. *Nonlinear Dyn.* **105**(1), 167–190 (2021)
31. Xiong, H., Kong, X., Yang, Z., et al.: Response regimes of narrow-band stochastic excited linear oscillator coupled to nonlinear energy sink. *Chin. J. Aeronaut. J. Aeronaut.* **28**(2), 457–468 (2015)
32. Shutong, F., Yongjun, S.: Research on a viscoelastic nonlinear energy sink under harmonic excitation. *Chinese J. Theor. Appl. Mech.* **54**(9), 2567–2576 (2022)
33. Yang, J., Xiong, Y.P., Xing, J.T.: Power flow behaviour and dynamic performance of a nonlinear vibration absorber coupled to a nonlinear oscillator. *Nonlinear Dyn.* **80**, 1063–1079 (2015)
34. AL-Shudeifat, M.A.: Nonlinear energy sinks with nontraditional kinds of nonlinear restoring forces. *J. Vib. Acoust. Vib. Acoust.* **139**(2), 024503 (2017)
35. Jing, X.J., Lang, Z.Q.: Frequency domain analysis of a dimensionless cubic nonlinear damping system subject to harmonic input. *Nonlinear Dyn.* **58**, 469–485 (2009)
36. Guo, P.F., Lang, Z.Q., Peng, Z.K.: Analysis and design of the force and displacement transmissibility of nonlinear viscous damper based vibration isolation systems. *Nonlinear Dyn.* **67**, 2671–2687 (2012)
37. Andersen, D., Starosvetsky, Y., Vakakis, A., et al.: Dynamic instabilities in coupled oscillators induced by geometrically nonlinear damping. *Nonlinear Dyn.* **67**, 807–827 (2012)
38. Andersen, D.K., Vakakis, A.F., Bergman, L.A.: Dynamics of a system of coupled oscillators with geometrically nonlinear damping. *Nonlinear Modeling and Applications, Volume 2: Proceedings of the 28th IMAC, A Conference on Structural Dynamics*, 2010. Springer New York, New York, NY, pp. 1–7 (2011). https://doi.org/10.1007/978-1-4419-9719-7_1
39. Ahmadabadi, Z.N., Khadem, S.E.: Annihilation of high-amplitude periodic responses of a forced two degrees-of-freedom oscillatory system using nonlinear energy sink. *J. Vib. Control Vib. Control* **19**(16), 2401–2412 (2013)
40. Yunfa, Z., Xianren, K.: Analysis on vibration suppression response of nonlinear energy sink with combined nonlinear damping. *Chinese J. Theor. Appl. Mech.* **55**(04), 972–981 (2023)
41. Fang, Z.W., Zhang, Y.W., Li, X., et al.: Complexification-averaging analysis on a giant magnetostrictive harvester integrated with a nonlinear energy sink. *J. Vib. Acoust. Vib. Acoust.* **140**(2), 021009 (2018)

Publisher's Note Springer Nature remains neutral with regard to jurisdictional claims in published maps and institutional affiliations.

Springer Nature or its licensor (e.g. a society or other partner) holds exclusive rights to this article under a publishing agreement with the author(s) or other rightsholder(s); author self-archiving of the accepted manuscript version of this article is solely governed by the terms of such publishing agreement and applicable law.